Doctoral Dissertation

Control and Mechanism Design of Nonlinear Systems Controllable with First-order Lie Brackets

Yuki Takagi

June 2023

Graduate School of Engineering, Osaka University

Acknowledgement

本研究は 2019 年 4 月から 2023 年 9 月の期間において、大阪大学大学院工学研究科機械工学専攻において石川将人教授の指導の下で行われました。この博士学位論文の完成にあたり、多くの方々から助けと指導をいただきましたことを心から感謝申し上げます。

　まず、石川将人教授には、貴重なご指導とご鞭撻をいただきましたことに深く感謝いたします。石川先生の熱心なご指導は、私の研究を大いに深める助けとなりました。

　また、南裕樹准教授と増田容一助教には、研究室での日々の研究活動において的確なアドバイスと温かなご支援をいただきましたことに感謝いたします。南先生の貴重な訓告と、増田先生の熱心な助力は私の研究を大いに促進し、常に励ましとなりました。

　さらに、佐藤訓志教授、東森充教授、南裕樹准教授には、貴重なご意見をいただきましたことに深く感謝申し上げます。ご教示いただいた助言は、論文の品質向上に大いに寄与しました。

　博士前期課程においては、大須賀・杉本研究室のメンバーの皆様に多大なる協力をいただきました。皆様のご支援と協力に心より感謝いたします。

　また、以前の職場であるナノフォトン株式会社、特に河田聡氏、小林実氏、塩崎祐介氏には、貴重な経験と知識を授けていただきましたことに深く感謝いたします。この助力は本学位論文の完成に不可欠なものでした。

　最後になりますが、友人や家族には、いつも私を支えてくれる温かな応援と励ましをいただきましたことに心から感謝いたします。

Contents

List of Figures

Chapter 1

Introduction

This thesis addresses the control and mechanics of first-order Lie bracket systems, a class of nonholonomic systems. A major class of nonholonomic systems is those that are subject to a form of constraint

$$
\begin{bmatrix} \boldsymbol{c_1^\mathsf{T}}(\boldsymbol{q}) \\ \vdots \\ \boldsymbol{c_m^\mathsf{T}}(\boldsymbol{q}) \end{bmatrix} \cdot \dot{\boldsymbol{q}} = \boldsymbol{0},
\tag{1.1}
$$

where $\boldsymbol{q} \in \mathbb{R}^n$ denotes the state vector and $\boldsymbol{c_1}(\boldsymbol{q}), \ \ldots, \ \boldsymbol{c_m}(\boldsymbol{q}) \in \mathbb{R}^n$ denote constraint vectors. The term *nonholonomic* means that the differential equation (1.1) is not integrable, hence it cannot be expressed in the form of $\boldsymbol{h}(\boldsymbol{q}) = $ constant. Nonholonomic systems can potentially change these full configurations from an arbitrary point to another one through the less number of instantaneous degrees of freedom. For example, in the case of a differential-drive vehicle, it is possible to change its position and orientation (three degrees of freedom in total) from any initial state to another, by appropriately choosing the velocity of two wheels. Considering the admissible velocity to be the control input, this mechanical property is interpreted as the controllability of nonlinear systems. Here, even if controllability is guaranteed, it is not trivial to find a time sequence of input. This is because, due to the constraint (1.1), the set of admissible velocities $\dot{\boldsymbol{q}}$ does not span $T_q\mathbb{R}^n = \mathbb{R}^n$. In a differential-drive vehicle, any wheel velocity cannot achieve lateral sliding motion.

These controllable underactuated systems would have some advantages and possible applications, as discussed in [2]. On the other hand, its control is much more difficult than that of fully actuated systems. It is unsolved even for the path planning problems before discussing the robustness and other issues, which restricts the potential for use. Therefore, this study addresses the path planning problem on underactuated systems with nonholonomic constraints.

Now we classify the symmetric affine systems form a viewpoint of the Lie bracket, an operation on vector fields that characterizes the structure of nonlinear controllability. Systems that are not controllable will not be considered. Among these systems, the smallest state dimension is three, whose controllability is ensured by two inputs and a unique first-order Lie bracket by the inputs. All other symmetric affine systems can be viewed as extensions of the two-input three-state dimension systems in the direction of depth or breadth, or both. Here, depth-extended systems denote systems that are controllable by higher-order Lie brackets, such as the "chained system." Breadth-extended systems are called the "first-order systems," in which n-dimensional states are controllable by m inputs and their first-order Lie brackets.

I focus on the first order systems according to its *delay*. The *delay* here refers to the required steps of time integration from the input to the state . It is analogous to the relative

degree of the linear SISO systems. The first-order systems have the smallest *delay* in the underactuated systems. In control engineering for mechanical systems, not in general control theory, it is loosely shared that control of systems with high deley tends to cause inconvenience, and I agree with this idea. Therefore, I decided to focus on first-order systems to contribute to social implementations of nonholonomic systems. As an engineering major, the significance of addressing control problems in nonholonomic systems, which have been the focus of mathematicians, lies precisely on this point.

This thesis consists of five chapters. In Chapter 1, I have described the focus of this thesis and its motivation.

Chapter 2 describes the Lie bracket and nonlinear control theory. The first-order systems are defined according to this background theory. This is also the basis of the following two contributions.

Chapter 3 describes the contributions to control theory. This chapter addresses an optimal path planning problem on the three-input six-dimensional Brockett's canonical system. By introducing the input quadratic norm as a Riemannian metric, we show that the shortest paths connecting two points are parametrized as helix paths. In addition, we present a quasi-analytical procedure to determine the optimal helix path for any given target point. The characteristic feature of our method is that the optimal paths are parametrized as an explicit function on the state space, which enables the solution paths to be derived without multi-dimensional iterations. The approach is validated by numerical computations in two aspects: matching for arbitrary target points and covering known optimal paths as special cases.

Chapter 4 describes the contributions to mechanism design. This chapter introduces the notion of a *kinematic-dual snake robot*, as contrasted with a *conventional* wheeled snake robot. The well-known snake robot consists of active joints and passive wheels corresponding side-slip constraints. The purpose of this study is to present a string-like mobile mechanism as a solution to the difficulty of manipulating the original snake. The key idea in devising the proposed snake is to reverse the mechanical elements of the original snake and then refine the reversed mechanism by the kinematics so that it is a dual system of the original snake. Thus, the proposed snake consists of passive joints and active omnidirectional wheels plus two ordinary wheels at the ends, associated with side-slip constraints. Here, we introduce the concept of the kinematic-dual snake and explain in what sense it is *kinematic-dual*. Then, through controllability analysis, motion planning, and experiments, we prove that the concept of the kinematic-dual snake is reliable as a mobile mechanism. The proposed robot can improve its manipulability while maintaining the advantages of the string-like body. The authors expect this idea would contribute to tasks that require both joint angle manipulation and traveling, such as transportation with wrapping around an object.

Chapter 5 summarizes the contributions of this thesis and their significance.

Chapter 2

Nonlinear Controllability and its Characterization Using Lie brackets

This chapter describes the Lie bracket, an operation on vector fields that characterizes the structure of nonlinear controllability. These discussions are summarized in the following books: nonlinear control theory[3, 4]; control of nonholonomic systems[5, 6].

Among the nonholonomic systems, this study considers symmetric affine systems of the form

$$\dot{\boldsymbol{q}} = \sum_{i=1}^{m} \boldsymbol{g_i}(\boldsymbol{q}) u_i, \quad \boldsymbol{q}, \ \boldsymbol{g_i}(\boldsymbol{q}) \in \mathbb{R}^n, \tag{2.1}$$

where $\boldsymbol{q}$ denotes the state, u_i denotes the input. The vector field $\boldsymbol{g_i}(\boldsymbol{q})$ indicates direction of state change driven by the input. Many mechanical systems such that the nonholonomic constraints (1.1) correspond to the generalized velocities are represented as this symmetric affine system.

The following definition of nonlinear controllability is widely used, and this thesis follows this.

Definition 1. *Nonlinear controllability[7]: The nonlinear system* (2.1) *is said to be controllable if, for any pair of* $\boldsymbol{q_0}$, $\boldsymbol{q_f}$, *there exists a finite time* T *and an admissible control input* $\boldsymbol{u}(t)$ *defined on the interval* $[0, T]$ *such that the resulting solution* $\boldsymbol{q}(t)$ *starting from* $\boldsymbol{q}(0) = \boldsymbol{q_0}$ *satisfies* $\boldsymbol{q}(t) = \boldsymbol{q_f}$.

A prominent way to prove the nonlinear controllability is using a product operation called the Lie bracket. For two smooth vector fields $\boldsymbol{g_i}(\boldsymbol{q}), \boldsymbol{g_j}(\boldsymbol{q}) \in \mathbb{R}^n$, the operation

$$[\boldsymbol{g_i}(\boldsymbol{q}), \boldsymbol{g_j}(\boldsymbol{q})] := \frac{\partial \boldsymbol{g_j}(\boldsymbol{q})}{\partial \boldsymbol{q}} \cdot \boldsymbol{g_i}(\boldsymbol{q}) - \frac{\partial \boldsymbol{g_i}(\boldsymbol{q})}{\partial \boldsymbol{q}} \cdot \boldsymbol{g_j}(\boldsymbol{q}) \tag{2.2}$$

is Lie bracket of $\boldsymbol{g_i}(\boldsymbol{q})$ and $\boldsymbol{g_j}(\boldsymbol{q})$. The Lie bracket itself is also a vector field on $\mathbb{R}^n$. Thus we can consider a recursive Lie bracket such as $[\boldsymbol{g_i}(\boldsymbol{q}), [\boldsymbol{g_i}(\boldsymbol{q}), \boldsymbol{g_j}(\boldsymbol{q})]]$, and can repeat this operation for infinitely many times. The following theorem describes a computable condition of nonlinear controllability of the symmetric affine systems using the Lie brackets.

Theorem 1. *Chow's theorem: The system* (2.1) *is controllable if and only if* $\boldsymbol{g_i}(\boldsymbol{q})$ *and these recurrent Lie brackets span the dimension* n *for all* $\boldsymbol{q}$.

Note that even if the system is *controllable in the nonlinear sense*, we cannot move the state $\boldsymbol{q}$ in all directions instantaneously (these motions require $[\boldsymbol{g_1}(\boldsymbol{q}) \ \boldsymbol{g_2}(\boldsymbol{q}) \ \cdots \ \boldsymbol{g_m}(\boldsymbol{q})]$ to be full
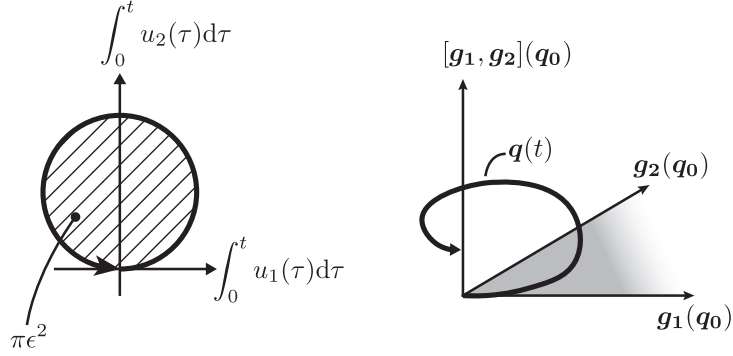
Fig. 2.1 The left-side figure shows the path of the input (2.3). The area enclosed by the path on the time integration of the u_1 and u_2 plane equals $\pi\epsilon^2$. With this input, state $\boldsymbol{q}(t)$ traces the path shown in the right-side figure. The state $\boldsymbol{q}$ moves not only in the plane formed by $\boldsymbol{g_1}(\boldsymbol{q_0})$ and $\boldsymbol{g_2}(\boldsymbol{q_0})$, but also in the direction of $[\boldsymbol{g_1}(\boldsymbol{q_0}), \boldsymbol{g_2}(\boldsymbol{q_0})]$, because the vector $\boldsymbol{g_i}(\boldsymbol{q})$ changes as the state $\boldsymbol{q}$ changes.

row rank); we can only move the state $\boldsymbol{q}$ to a position in finite time with finite input.

Let us mention a geometric meaning of the Lie bracket. The Lie bracket $[\boldsymbol{g_i}, \boldsymbol{g_j}]$ means the direction of state change caused by a periodic control by two corresponding inputs, with a small amplitude and a phase difference. For example, applying the input

$$(u_1(t), u_2(t)) = \left(\epsilon \frac{2\pi}{T} \cos\left(\frac{2\pi t}{T}\right), \epsilon \frac{2\pi}{T} \sin\left(\frac{2\pi t}{T}\right) \right) \tag{2.3}$$

moves the state from $\boldsymbol{q}(0) = \boldsymbol{q_0}$ to $\boldsymbol{q}(T)$ as

$$\boldsymbol{q}(T) = \boldsymbol{q_0} + \pi\epsilon^2 \left(\frac{\partial \boldsymbol{g_2}(\boldsymbol{q})}{\partial \boldsymbol{q}} \boldsymbol{g_1}(\boldsymbol{q}) - \frac{\partial \boldsymbol{g_1}(\boldsymbol{q})}{\partial \boldsymbol{q}} \boldsymbol{g_2}(\boldsymbol{q}) \right)\Bigg|_{\boldsymbol{q_0}} + \boldsymbol{O}(\epsilon^3). \tag{2.4}$$

Figure 2.1 shows the path of the input (2.3) and the path of the state with the input (2.3). The direction of the displacement from $\boldsymbol{q}(0)$ to $\boldsymbol{q}(T)$ corresponds to the Lie bracket of a pair of vector fields, since the Lie bracket is defined as (2.2).

Chapter 3

Optimal Path Planning on the Three-Input Six-Dimensional Brockett's Canonical System

3.1 Introduction: Finite-time steering of first-order systems

3.1.1 Related works: Finite time steering methods for "first-order systems"

This section introduces existing path planning methods that include first-order systems as their target systems and classifying them in two aspects: rate of decay and representations of the target systems. There are many path planning methods based on Lyapunov's stability theory in which the time evolution of state quantities decays exponentially (or its extension), e.g., [8, 9, 10, 11, 12, 13]. However, we focus on finite-time steering, which is a stronger result than exponential stabilization. If finite-time steering is achieved, the system is exponentially stable, but the converse is not always true. We note that finite-time steering is not always superior to exponential stabilization as a controller.

Several finite-time steering methods are proposed in [1, 14, 15]. Murray[1] presents a step-by-step steering method on the first-order canonical systems introduced in [16]. Due to the difficulty of matching multiple state variables to boundary conditions by the optimal paths, they divide the state steering into some steps based on controllability structure. Leonard[14] expands the target system to matrix Lie groups and provides a steering method similar to [1]. Matrix Lie groups can represent Brockett's canonical system without any defect and include the matrix representations of $\mathbb{SO}(m)$ and $\mathbb{SE}(m)$, which are important for application use. The behavior of these step-by-step steering for a differential-drive vehicle is shown schematically in Fig. 3.1. In the words of [14], step-by-step steering is a "constructive controllability" method and is not the result of aiming to gain a *good* path but only to steer in finite time. Although there are various measures of good paths, the authors feel it natural to minimize the path length by introducing the inputs as a Riemannian metric.

This input Riemannian metric minimization problem was tackled early on by Brockett[17, 16] and Baillieul[18]. The formulation of these optimization problems is summarized in [19]. Jurdjevic[20, 21] also dealt with this problem in a mathematical manner. In [16], Brockett introduced a local canonical system for the first-order controllable systems. In addition to introducing the canonical system, Brockett parametrizes the optimal inputs by solving the optimization problem. This result plays an important role in this study and will be discussed in detail in Section 3.3.
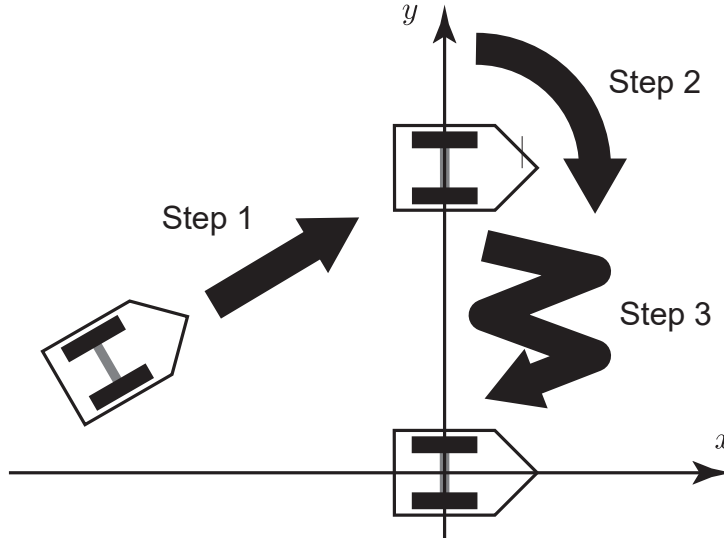
Fig. 3.1 A schematic sequence of steering a differential-drive vehicle by the method presented in [1]. Step 1: Steer x-coordinate to zero by forwarding motion. Step 2: Steer θ-coordinate to zero by rotation. Step 3: Steer y-coordinate to zero by combining forward/backward motion and rotation. Each state quantity is steered in a separate step. The motion is not aimed at its optimality.

Several methods to obtain specific optimal paths have been presented by using the above formulation or numerical computations. A numerical computation method was reported in [22]. Using the existing result that the optimal paths on $\mathbb{SO}(3)$ are parametrized as elliptic functions, Spindler[23] uses the shooting method to match the boundary conditions. Henninger[24] extend the target system to include $\mathbb{SO}$ groups and provide similar results to [23]. In three-dimensional systems, they also present an analytic method. The authors of [25] and [26] focused on a particular system on $\mathbb{SE}(3)$. Both authors discuss optimal orientation problems at unit speeds intended for airplanes, and helix paths are derived as the solution paths.

3.1.2 The focus of the chapter

In summary, for the case of more than three-dimensional systems, either step-by-step steering, a "constructive controllability" method, or multi-dimensional numerical optimization is required. A more powerful result, finding the shortest path by an analytical procedure, has only been achieved for two-input three-dimensional or specific systems. Hence, we address the optimal path planning on the three-input six-dimensional Brockett's canonical system.

The setting of the target system is limited but significant. Three-dimensional inputs can steer six-dimensional states maximally by the first-order Lie brackets, and six dimensions are identical to the degrees of freedom of $\mathbb{SE}(3)$. Precisely, it corresponds to controlling the position and orientation of a rigid body in three-dimensional space by three-dimensional inputs. Our focus on the canonical system will contribute as the first step toward solving more general problems since finite-time steering was first solved for the canonical systems and then extended to larger classes.

Our purpose is to present a parametric representation of the optimal paths and a path-

determining method for any given target point. To this end, in Section 3.3, we show that the set of *good* paths, meaning that the path length is the local minimum, can be parameterized as helix paths. In Section 3.4, the existence of helix paths that satisfy the boundary conditions for almost all target points and a determining method are presented. In Section 3.5, numerical examples show that the paths can be matched for many target points with reasonable accuracy. We also show that the helix paths introduced in Section 3.3 contain the global shortest paths for several specific target points. Finally, in Section 3.6, we summarize the contents of this chapter.

The position of this chapter relative to existing studies can be summarized as follows. [1, 14] are direct motivation of this study. They present finite-time steering methods for a wide class of systems but do not aim to gain *good* paths. In contrast, the path planning method in this study gains good paths in the sense that the path length measured by the input Riemannian metric is the local minimum. While there are numerical methods to plan the paths, this study not only presents a path planning method but also parametrizes the local optimal paths by helix.

3.2 Preliminaries

This section describes mathematical notations. If the reader is unfamiliar with these theorems, please see [27].

The cross product of two vectors $\boldsymbol{v},\ \boldsymbol{w} \in \mathbb{R}^3$ is defined as

$$\boldsymbol{v} \times \boldsymbol{w} := \begin{bmatrix} v_2 \cdot w_3 - v_3 \cdot w_2 \\ v_3 \cdot w_1 - v_1 \cdot w_3 \\ v_1 \cdot w_2 - v_2 \cdot w_1 \end{bmatrix}, \quad \boldsymbol{v} = \begin{bmatrix} v_1 \\ v_2 \\ v_3 \end{bmatrix}, \ \boldsymbol{w} = \begin{bmatrix} w_1 \\ w_2 \\ w_3 \end{bmatrix}. \tag{3.1}$$

Since the cross product by $\boldsymbol{v}$ is a linear operator, by defining wedge operator $(\cdot)^\wedge$ as

$$\widehat{\boldsymbol{v}} = (\boldsymbol{v})^\wedge = \begin{bmatrix} 0 & -v_3 & v_2 \\ v_3 & 0 & -v_1 \\ -v_2 & v_1 & 0 \end{bmatrix}, \tag{3.2}$$

we can represent the cross product as

$$\boldsymbol{v} \times \boldsymbol{w} = (\boldsymbol{v})^\wedge \cdot \boldsymbol{w}. \tag{3.3}$$

For a vector $\boldsymbol{\omega} \in \mathbb{R}^3$, $|\boldsymbol{\omega}| = 1$, the following equation holds:

$$(\widehat{\boldsymbol{\omega}})^2 = \boldsymbol{\omega}\boldsymbol{\omega}^\mathsf{T} - \boldsymbol{I}, \tag{3.4}$$

where $\boldsymbol{I}$ denotes the unit matrix. The following equation is held for the dot product and cross product of the vectors $\boldsymbol{u},\ \boldsymbol{v},\ \boldsymbol{w} \in \mathbb{R}^3$:

$$\boldsymbol{u}^\mathsf{T} \cdot (\boldsymbol{v} \times \boldsymbol{w}) = \boldsymbol{v}^\mathsf{T} \cdot (\boldsymbol{w} \times \boldsymbol{u}) = \boldsymbol{w}^\mathsf{T} \cdot (\boldsymbol{u} \times \boldsymbol{v}). \tag{3.5}$$

We define the normalization operator for the non -zero vectors as

$$\overline{\boldsymbol{v}} := \frac{\boldsymbol{v}}{|\boldsymbol{v}|}. \tag{3.6}$$

By using two ordered vectors $\boldsymbol{v}, \boldsymbol{w} \in \mathbb{R}^3$, $\boldsymbol{v} \times \boldsymbol{w} \neq \boldsymbol{0}$, we define the normal orthogonal coordinate system $\boldsymbol{C}(\boldsymbol{v}, \boldsymbol{w}) \in \mathbb{SO}(3)$ as

$$\boldsymbol{C}(\boldsymbol{v}, \boldsymbol{w}) := \begin{bmatrix} \overline{\boldsymbol{v}} & \overline{\boldsymbol{v} \times \boldsymbol{w}} & \overline{\boldsymbol{v} \times (\boldsymbol{v} \times \boldsymbol{w})} \end{bmatrix}. \tag{3.7}$$

Maps by $\boldsymbol{R} \in \mathbb{SO}(3)$ hold the following relations for the given $\boldsymbol{v}, \boldsymbol{w} \in \mathbb{R}^3$:

$$|\boldsymbol{R} \cdot (\boldsymbol{v} - \boldsymbol{w})| = |\boldsymbol{v} - \boldsymbol{w}|, \tag{3.8}$$

$$\boldsymbol{R} \cdot (\boldsymbol{v} \times \boldsymbol{w}) = (\boldsymbol{R} \cdot \boldsymbol{v}) \times (\boldsymbol{R} \cdot \boldsymbol{w}). \tag{3.9}$$

3.3 Parametrization of the optimal paths

This section discovers a set of candidates for *good* paths. For this purpose, we define an input Riemannian metric minimization problem between two points on the three-input six-dimensional Brockett's canonical system. We then derive a parametric path representation that satisfies the shortest stationary condition.

First, we define the minimization problem as follow:

Problem 1. *Primal optimization problem*

$$given\ \boldsymbol{x_f},\ \boldsymbol{y_f} \tag{3.10}$$

$$system\ \dot{\boldsymbol{x}} = \boldsymbol{u},\ \dot{\boldsymbol{y}} = \boldsymbol{x} \times \boldsymbol{u} \tag{3.11}$$

$$find\ \boldsymbol{x}(\tau),\ \tau \in [0, 1] \tag{3.12}$$

$$s.\ t.\ \boldsymbol{x}(0) = \boldsymbol{0},\ \boldsymbol{y}(0) = \boldsymbol{0},\ \boldsymbol{x}(1) = \boldsymbol{x_f},\ \boldsymbol{y}(1) = \boldsymbol{y_f} \tag{3.13}$$

$$minimize\ J = \int_0^1 \boldsymbol{u}^\mathsf{T} \cdot \boldsymbol{u}\mathrm{d}\tau \tag{3.14}$$

Where $\boldsymbol{x}, \boldsymbol{y} \in \mathbb{R}^3$ are state vectors, and let $\boldsymbol{x}$ and $\boldsymbol{y}$ be called base coordinates and fiber coordinates, respectively. A pair of $\{\boldsymbol{x_f}, \boldsymbol{y_f}\}$ denotes a target point. $\boldsymbol{u}(\cdot) : [0, 1] \to \mathbb{R}^3$ denotes control input. In this formulation, we introduce the quadratic form $\boldsymbol{u}^\mathsf{T} \cdot \boldsymbol{u}$ as a Riemannian metric, not the input two-norm $\sqrt{\boldsymbol{u}^\mathsf{T} \cdot \boldsymbol{u}}$. These settings do not change the solution paths of the optimization problem [16], and these simplify reducing Problem 1 to Problem 2.

For this problem, the following theorem holds:

Theorem 2. *For the solutions of Problem 1 $\boldsymbol{x}^*(\tau)$, there exist constant vectors $\boldsymbol{\lambda_c}, \boldsymbol{v} \in \mathbb{R}^3$, such that the following equation holds:*

$$\frac{\mathrm{d}}{\mathrm{d}\tau}\boldsymbol{x}^*(\tau) = \boldsymbol{\gamma_\lambda}(\tau) \tag{3.15}$$

where $\boldsymbol{\gamma_\lambda} : [0, 1] \to \mathbb{R}^3$ is a parametric curve defined by

$$\boldsymbol{\gamma_\lambda}(\tau) := \exp(\widehat{\boldsymbol{\lambda_c}}\tau) \cdot \boldsymbol{v}\ (0 \leq \tau \leq 1). \tag{3.16}$$

Proof. This theorem was discussed for general dimensional case in [16], and a kind description is provided in [1]. Here we provide a proof specialized within 3-dimensional input.

The Lagrangian function of the evaluation function (3.14) and the constraint equation (3.11) is expressed as

$$L(\boldsymbol{x}, \dot{\boldsymbol{x}}, \boldsymbol{y}, \dot{\boldsymbol{y}}, \boldsymbol{\lambda}) = \dot{\boldsymbol{x}}^\mathsf{T} \cdot \dot{\boldsymbol{x}} + \boldsymbol{\lambda}^\mathsf{T} \cdot (\dot{\boldsymbol{y}} - \boldsymbol{x} \times \dot{\boldsymbol{x}}) \tag{3.17}$$

with the Lagrangian multiplier $\boldsymbol{\lambda} : [0,1] \mapsto \mathbb{R}^3$ and without $\boldsymbol{u}$. Solving the Euler-Lagrange equation for $\boldsymbol{y}$ yields

$$
\begin{aligned}
\boldsymbol{0} &= \frac{\mathrm{d}}{\mathrm{d}\tau} \left(\frac{\partial L}{\partial \dot{\boldsymbol{y}}} \right) - \frac{\partial L}{\partial \boldsymbol{y}} \\
&= \dot{\boldsymbol{\lambda}}.
\end{aligned}
\tag{3.18}
$$

Likewise, solving for $\boldsymbol{x}$ with substituting $\dot{\boldsymbol{\lambda}} = \boldsymbol{0}$ yields

$$
\begin{aligned}
\boldsymbol{0} &= \frac{\mathrm{d}}{\mathrm{d}\tau} \left(\frac{\partial L}{\partial \dot{\boldsymbol{x}}} \right) - \frac{\partial L}{\partial \boldsymbol{x}} \\
&= (2\ddot{\boldsymbol{x}} - \boldsymbol{\lambda} \times \dot{\boldsymbol{x}} - \dot{\boldsymbol{\lambda}} \times \boldsymbol{x}) - (\boldsymbol{\lambda} \times \dot{\boldsymbol{x}}) \\
&= 2\ddot{\boldsymbol{x}} - 2\boldsymbol{\lambda} \times \dot{\boldsymbol{x}}.
\end{aligned}
\tag{3.19}
$$

This differential equation can be solved by using the matrix exponential function as

$$
\dot{\boldsymbol{x}}(\tau) = \exp\left(\widehat{\boldsymbol{\lambda}}\tau\right) \cdot \dot{\boldsymbol{x}}(0).
\tag{3.20}
$$

$\square$

From here, we begin the original formulations. First, we normalize $\boldsymbol{\lambda_c}$ and impose its norm on the time.

Corollary 1. *For the parametric curve $\boldsymbol{\gamma_\lambda}$, there exist an equivalent parametric cruve $\boldsymbol{\gamma_\omega} : [0, t_f] \to \mathbb{R}^3$ defined by*

$$
\boldsymbol{\gamma_\omega}(t) := \exp(\widehat{\boldsymbol{\omega}}t) \cdot \boldsymbol{v} \quad (0 \le t \le t_f),
\tag{3.21}
$$

$$
\boldsymbol{\omega} \in \mathbb{R}^3, \ |\boldsymbol{\omega}| = 1.
\tag{3.22}
$$

Due to the equivalence of $\boldsymbol{\gamma_\omega}$ and $\boldsymbol{\gamma_\lambda}$, integrating $\boldsymbol{\gamma_\omega}$ on the time yield another parametric curve that is equivalent to the solution curve of Problem 1 $\boldsymbol{x}^*(\tau)$.

We can observe that $\exp(\widehat{\boldsymbol{\omega}}t) \cdot \boldsymbol{v}$ represents the rotation of a constant vector $\boldsymbol{v}$ about an axis $\boldsymbol{\omega}$ for an angle t. This geometric observation leads us to express (3.21) as the following time-integrated form.

Theorem 3. *For the constant vectors $\boldsymbol{\omega}, \boldsymbol{v} \in \mathbb{R}^3$, satisfying $|\boldsymbol{\omega}| = 1$, there exist $r, h \in \mathbb{R}$, $r \ge 0$, $\boldsymbol{\Omega} \in \mathbb{SO}(3)$ such that the following equation holds:*

$$
\boldsymbol{\xi}_{r,h}(t) := \begin{bmatrix} ht \\ r \cdot \sin t \\ r \cdot (1 - \cos t) \end{bmatrix}, \quad \boldsymbol{\xi}_{r,h}(\cdot) : [0, t_f] \to \mathbb{R}^3,
\tag{3.23}
$$

$$
\int_0^t \exp(\widehat{\boldsymbol{\omega}}\tau) \cdot \boldsymbol{v} \mathrm{d}\tau = \boldsymbol{\Omega} \cdot \boldsymbol{\xi}_{r,h}(t).
\tag{3.24}
$$

Proof. The Rodrigues' rotation formula expand $\exp(\widehat{\boldsymbol{\omega}}\tau) \cdot \boldsymbol{v}$ as

$$
\exp(\widehat{\boldsymbol{\omega}}\tau) \cdot \boldsymbol{v} = \boldsymbol{v} + \widehat{\boldsymbol{\omega}}\boldsymbol{v}\sin(\tau) + \widehat{\boldsymbol{\omega}}^2\boldsymbol{v}(1 - \cos(\tau))
\tag{3.25}
$$

$$
= (\boldsymbol{\omega}^\mathsf{T}\boldsymbol{v})\boldsymbol{\omega} - \widehat{\boldsymbol{\omega}}^2\boldsymbol{v}\cos(\tau) + \widehat{\boldsymbol{\omega}}\boldsymbol{v}\sin(\tau).
\tag{3.26}
$$

If $\widehat{\boldsymbol{\omega}}\boldsymbol{v} \neq 0$, then we can re-arrange $\exp(\widehat{\boldsymbol{\omega}}\tau) \cdot \boldsymbol{v}$ as

$$\exp(\widehat{\boldsymbol{\omega}}\tau) \cdot \boldsymbol{v} = \begin{bmatrix} \boldsymbol{\omega} & -\overline{\widehat{\boldsymbol{\omega}}^2\boldsymbol{v}} & \overline{\widehat{\boldsymbol{\omega}}\boldsymbol{v}} \end{bmatrix} \cdot \begin{bmatrix} \boldsymbol{\omega}^\mathsf{T}\boldsymbol{v} \\ |\widehat{\boldsymbol{\omega}}^2\boldsymbol{v}|\cos(\tau) \\ |\widehat{\boldsymbol{\omega}}\boldsymbol{v}|\sin(\tau) \end{bmatrix}. \tag{3.27}$$

Here we can verify the followings:

$$\begin{bmatrix} \boldsymbol{\omega} & -\overline{\widehat{\boldsymbol{\omega}}^2\boldsymbol{v}} & \overline{\widehat{\boldsymbol{\omega}}\boldsymbol{v}} \end{bmatrix}^\mathsf{T} \cdot \begin{bmatrix} \boldsymbol{\omega} & -\overline{\widehat{\boldsymbol{\omega}}^2\boldsymbol{v}} & \overline{\widehat{\boldsymbol{\omega}}\boldsymbol{v}} \end{bmatrix} = \boldsymbol{I}, \tag{3.28}$$

$$\det \begin{bmatrix} \boldsymbol{\omega} & -\overline{\widehat{\boldsymbol{\omega}}^2\boldsymbol{v}} & \overline{\widehat{\boldsymbol{\omega}}\boldsymbol{v}} \end{bmatrix} = 1, \tag{3.29}$$

$$|\widehat{\boldsymbol{\omega}}^2\boldsymbol{v}| = |\widehat{\boldsymbol{\omega}}\boldsymbol{v}|. \tag{3.30}$$

Therefore, if $\widehat{\boldsymbol{\omega}}\boldsymbol{v} \neq 0$, there exist $r \geq 0$, $h \in \mathbb{R}$, $\boldsymbol{\Omega} \in \mathbb{SO}(3)$ such that

$$\exp(\widehat{\boldsymbol{\omega}}\tau) \cdot \boldsymbol{v} = \boldsymbol{\Omega} \cdot \begin{bmatrix} h \\ r\cos(\tau) \\ r\sin(\tau) \end{bmatrix} \tag{3.31}$$

is held. For the excepted cases, such that $\widehat{\boldsymbol{\omega}}\boldsymbol{v} = 0$, we can also verify the existence of such $\{r,\ h,\ \boldsymbol{\Omega}\}$.

Since $\boldsymbol{\Omega}$ is constatnt against the time, (3.31) can be integrated on the time interval $[0, t]$ as

$$\int_0^t \boldsymbol{\Omega} \cdot \begin{bmatrix} h \\ r\cos(\tau) \\ r\sin(\tau) \end{bmatrix} \mathrm{d}\tau = \boldsymbol{\Omega} \cdot \boldsymbol{\xi}_{r,h}(t). \tag{3.32}$$

$\square$

To summarize, the infinite-dimensional optimization problem defined as Problem 1 was reduced to the following boundary value problem with the evaluation function.

Problem 2. *Boundary value problem with evaluation function*

$$given\ \boldsymbol{x_f},\ \boldsymbol{y_f} \tag{3.33}$$

$$system\ \dot{\boldsymbol{x}} = \boldsymbol{u},\ \dot{\boldsymbol{y}} = \boldsymbol{x} \times \boldsymbol{u} \tag{3.34}$$

$$find\ \boldsymbol{\Omega} \in \mathbb{SO}(3),\ r,h,t_f \in \mathbb{R},\ r \geq 0,\ t_f \geq 0 \tag{3.35}$$

$$s.\ t.\ \boldsymbol{y}(0) = \boldsymbol{0},\ \boldsymbol{x}(t_f) = \boldsymbol{x_f},\ \boldsymbol{y}(t_f) = \boldsymbol{y_f}, \tag{3.36}$$

$$\boldsymbol{x}(t) = \boldsymbol{\Omega} \cdot \begin{bmatrix} ht \\ r \cdot \sin t \\ r \cdot (1 - \cos t) \end{bmatrix} \tag{3.37}$$

$$minimize\ J = \int_0^{t_f} \boldsymbol{u}^\mathsf{T} \cdot \boldsymbol{u}\mathrm{d}t \tag{3.38}$$

We note that Theorem 2 gives the local optimal paths, not the global optimal paths. If the admissible solutions of Problem 2 are unique against the given target points, the admissible solutions are the global optimal paths. However, there exist multiple admissible solutions if $|\boldsymbol{y_f}|$ is relatively large. Hence, we would evaluate J to find the global optimal paths among the admissible solutions.

While it is interesting to find the path that minimizes the evaluation function J among the admissible solutions, we do not aim to solve this problem but use the helix trajectory (3.37)

as a set of candidates for good paths. Conversely to the uniqueness, the existence of the helix paths that steer the system to almost all target points will be proved constructively in the next section.

3.4 Determination method of the optimal helix paths

This section provides the method for finding the optimal helix paths which match the boundary conditions. For simplicity, we assume the target points satisfy $\boldsymbol{x_f}^\mathsf{T} \cdot \boldsymbol{y_f} \neq 0$, $\boldsymbol{x_f} \times \boldsymbol{y_f} \neq \boldsymbol{0}$.

3.4.1 Representation of the helix orientation $\boldsymbol{\Omega}$

First, we solve about the orientation $\boldsymbol{\Omega}$ by considering its symmetries on $\mathbb{SO}(3)$ and obtain its explicit representation as a function of $\{r, h, t_f\}$ and $\{\boldsymbol{x_f}, \boldsymbol{y_f}\}$. By substituting the optimal base trajectory (3.37) into the system constraints (3.34), the behavior of the fiber coordinates $\boldsymbol{y}(t)$ is expressed as

$$\boldsymbol{y}(t) = \boldsymbol{y}(0) + \int_0^t \boldsymbol{x}(\tau) \times \boldsymbol{u}(\tau)\mathrm{d}\tau \tag{3.39}$$

$$= \int_0^t (\boldsymbol{\Omega} \cdot \boldsymbol{\xi}_{r,h}(\tau)) \times (\boldsymbol{\Omega} \cdot \dot{\boldsymbol{\xi}}_{r,h}(\tau))\mathrm{d}\tau \tag{3.40}$$

$$= \int_0^t \boldsymbol{\Omega} \cdot (\boldsymbol{\xi}_{r,h}(\tau) \times \dot{\boldsymbol{\xi}}_{r,h}(\tau))\mathrm{d}\tau \tag{3.41}$$

$$= \boldsymbol{\Omega} \cdot \int_0^t \boldsymbol{\xi}_{r,h}(\tau) \times \dot{\boldsymbol{\xi}}_{r,h}(\tau)\mathrm{d}\tau \tag{3.42}$$

$$= \boldsymbol{\Omega} \cdot \boldsymbol{\eta}_{r,h}(t), \tag{3.43}$$

where

$$\boldsymbol{\eta}_{r,h}(t) := \begin{bmatrix} r^2 \cdot (t - \sin t) \\ rh \cdot (t - 2\sin t + t\cos t) \\ rh \cdot (t\sin t + 2\cos t - 2) \end{bmatrix}. \tag{3.44}$$

Since $\boldsymbol{\Omega} \in \mathbb{SO}(3)$ is a rotation matrix, which preserve the distance and angle, a set of necessary conditions for $\{r, h, t_f\}$ to satisfy the boundary condition (3.36) is obtained as

$$\begin{aligned} |\boldsymbol{x_f}| &= |\boldsymbol{\xi}_{r,h}(t_f)|, \\ |\boldsymbol{y_f}| &= |\boldsymbol{\eta}_{r,h}(t_f)|, \\ \boldsymbol{x_f}^\mathsf{T} \cdot \boldsymbol{y_f} &= \boldsymbol{\xi}_{r,h}(t_f)^\mathsf{T} \cdot \boldsymbol{\eta}_{r,h}(t_f). \end{aligned} \tag{3.45}$$

Conversely, if (3.45) is satisfied, the boundary conditions can be matched by determining $\boldsymbol{\Omega}$ as

$$\boldsymbol{\Omega} = \boldsymbol{C}(\boldsymbol{x_f}, \boldsymbol{y_f}) \cdot (\boldsymbol{C}(\boldsymbol{\xi}_{r,h}(t_f), \boldsymbol{\eta}_{r,h}(t_f)))^{-1}. \tag{3.46}$$

This can be verified by the equations (3.37) and (3.43). Therefore, finding the admissible solutions of Problem 2 is reduced to the following three parameter problem:

Problem 3. *Reduced boundary value problem*

$$\text{given } \boldsymbol{x_f}, \ \boldsymbol{y_f}, \ \boldsymbol{x_f}^\mathsf{T} \cdot \boldsymbol{y_f} \neq 0, \ \boldsymbol{x_f} \times \boldsymbol{y_f} \neq 0 \tag{3.47}$$

$$\text{find } r, h, t_f \in \mathbb{R}, \ r \geq 0, \ t_f \geq 0 \tag{3.48}$$

$$\text{s.t. } \boldsymbol{\xi}_{r,h}(t) := \begin{bmatrix} ht \\ r \cdot \sin t \\ r \cdot (1 - \cos t) \end{bmatrix}, \tag{3.49}$$

$$\boldsymbol{\eta}_{r,h}(t) := \begin{bmatrix} r^2 \cdot (t - \sin t) \\ rh \cdot (t - 2\sin t + t\cos t) \\ rh \cdot (t\sin t + 2\cos t - 2) \end{bmatrix}, \tag{3.50}$$

$$|\boldsymbol{x_f}| = |\boldsymbol{\xi}_{r,h}(t_f)|, \ |\boldsymbol{y_f}| = |\boldsymbol{\eta}_{r,h}(t_f)|, $$
$$\boldsymbol{x_f}^\mathsf{T} \cdot \boldsymbol{y_f} = (\boldsymbol{\xi}_{r,h}(t_f))^\mathsf{T} \cdot \boldsymbol{\eta}_{r,h}(t_f) \tag{3.51}$$

3.4.2 Solving r, h, t_f by the given target points $\boldsymbol{x_f}, \boldsymbol{y_f}$

Next, we will solve the Problem 3 with respect to r, h, t_f, for the given conditions $\boldsymbol{x_f}, \ \boldsymbol{y_f}$. Let θ be the angle between them, which satisfies

$$\cos\theta = \frac{\boldsymbol{x_f}^\mathsf{T} \cdot \boldsymbol{y_f}}{|\boldsymbol{x_f}||\boldsymbol{y_f}|}. \tag{3.52}$$

In order to simplify the expression, we prepare the following functions of t:

$$a(t) := 2(1 - \cos t),$$
$$b(t) := t^2,$$
$$c(t) := (t - \sin t)^2,$$
$$d(t) := 2t^2 \cos t + 2t^2 - 8t\sin t - 8\cos t + 8,$$
$$e(t) := t^2 + t\sin t + 4\cos t - 4,$$
$$f(t) := 2t\sin t - 4(1 - \cos t) - t(t - \sin t).$$

From the conditions (3.51), we obtain

$$|\boldsymbol{x_f}|^2 = a(t_f)r^2 + b(t_f)h^2, \tag{3.53}$$

$$|\boldsymbol{y_f}|^2 = c(t_f)r^4 + d(t_f)r^2h^2, \tag{3.54}$$

$$|\boldsymbol{x_f}||\boldsymbol{y_f}|\cos\theta = e(t_f)r^2h. \tag{3.55}$$

We begin to express r and h as functions of t_f. The equations (3.53), (3.54) are summarized as

$$\begin{bmatrix} r^2|\boldsymbol{x_f}|^2 \\ |\boldsymbol{y_f}|^2 \end{bmatrix} = \begin{bmatrix} a(t_f) & b(t_f) \\ c(t_f) & d(t_f) \end{bmatrix} \begin{bmatrix} r^4 \\ r^2h^2 \end{bmatrix}. \tag{3.56}$$

The right-hand side is invertible since $ad - bc = ef < 0$ for any $t > 0$, then we obtain

$$\begin{bmatrix} r^4 \\ r^2h^2 \end{bmatrix} = \frac{1}{e(t_f)f(t_f)} \begin{bmatrix} d(t_f) & -b(t_f) \\ -c(t_f) & a(t_f) \end{bmatrix} \begin{bmatrix} r^2|\boldsymbol{x_f}|^2 \\ |\boldsymbol{y_f}|^2 \end{bmatrix}. \tag{3.57}$$

The first row is a quadratic equation with respect to r^2, i.e.,

$$r^4 - \frac{d(t_f)|\boldsymbol{x_f}|^2}{e(t_f)f(t_f)}r^2 + \frac{b(t_f)|\boldsymbol{y_f}|^2}{e(t_f)f(t_f)} = 0$$

is obtained. Since the last term $(b|\boldsymbol{y_f}|^2)/(ef) < 0$ for any $t > 0$, there exists a unique positive real solution with respect to r^2. Moreover, r must be positive by its definition. Therefore, r has a unique solution for t_f as

$$r(t_f) = \left. \sqrt{\frac{d|\boldsymbol{x_f}|^2}{2ef}\left(1 - \sqrt{1 - \frac{4bef|\boldsymbol{y_f}|^2}{d^2|\boldsymbol{x_f}|^4}}\right)}\right|_{t=t_f}. \tag{3.58}$$

By substituting this into (3.55), we have

$$h(t_f) = \frac{|\boldsymbol{x_f}||\boldsymbol{y_f}|\cos\theta}{(r(t_f))^2 \cdot e(t_f)}. \tag{3.59}$$

Finally, we solve t_f by $|\boldsymbol{x_f}|$, $|\boldsymbol{y_f}|$, and the angle θ. Substituting (3.59) into the second row of (3.57) leads

$$-cer^4|\boldsymbol{x_f}|^2 + aer^2|\boldsymbol{y_f}|^2 - f \cdot (|\boldsymbol{x_f}||\boldsymbol{y_f}|\cos\theta)^2\big|_{t=t_f} = 0. \tag{3.60}$$

Substituting (3.58) to eliminate r from (3.60), we obtain

$$(a^2b)\left(ef\frac{|\boldsymbol{y_f}|^2}{|\boldsymbol{x_f}|^4}\right)^2$$
$$+ ((f\cos\theta)^4 - (ad + 2bc)(f\cos\theta)^2 - bc(ad - bc))\left(ef\frac{|\boldsymbol{y_f}|^2}{|\boldsymbol{x_f}|^4}\right)$$
$$+ cd^2(f\cos\theta)^2\big|_{t=t_f}$$
$$= 0. \tag{3.61}$$

Solving (3.61) as a quadratic equation with respect to $\left(ef\dfrac{|\boldsymbol{y_f}|^2}{|\boldsymbol{x_f}|^4}\right)$, we have a function that gives its root as the t_f to be solved as

$$\frac{|\boldsymbol{y_f}|^2}{|\boldsymbol{x_f}|^4} - \frac{\beta_\theta \pm \gamma_\theta}{\alpha}(t), \tag{3.62}$$

where

$$\alpha(t) := 2a^2bef,$$
$$\beta_\theta(t) := -(f\cos\theta)^4 + (ad + 2bc)\cdot(f\cos\theta)^2 + bc\cdot(ad - bc),$$
$$\gamma_\theta(t) := (bc - (f\cos\theta)^2)\sqrt{((f\cos\theta)^2 - e^2)\cdot((f\cos\theta)^2 - f^2)}.$$

In order to find a t_f for any given $\boldsymbol{x_f}$ and $\boldsymbol{y_f}$, we expect the range of the functions $(\beta_\theta + \gamma_\theta)/\alpha$ and $(\beta_\theta - \gamma_\theta)/\alpha$ cover $[0, \infty)$ by a domain of t. This is proven as follows, with the aid of the intermediate value theorem. Figure 3.2 shows an overview of the functions $(\beta_\theta \pm \gamma_\theta)/\alpha$. Let

$$T_d := \min\{t > 0 \mid d(t) = 0\} \simeq 9.0, \tag{3.63}$$
$$t_\theta := \min\{t > 0 \mid \gamma_\theta(t) = 0\}, \quad \exists t_\theta \in (0, 2\pi), \ \forall|\cos\theta| \in (0, 1). \tag{3.64}$$
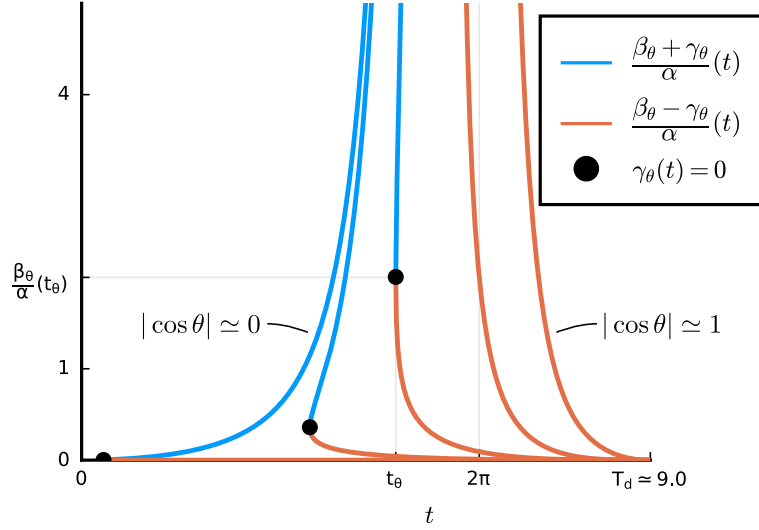
Fig. 3.2   The functions $(\beta_\theta \pm \gamma_\theta)/\alpha$ against t, for various values of θ. The bullet marks point at which $\gamma_\theta(t) = 0$. The functions $(\beta_\theta \pm \gamma_\theta)/\alpha$ ranges $[0, \infty)$ by $t \in (0, T_d]$, $\forall \theta$.
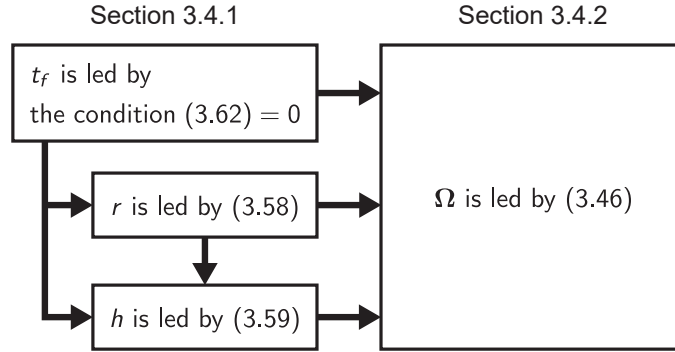
Fig. 3.3   Procedure for determining the optimal helix paths for the given $\{\boldsymbol{x_f}, \boldsymbol{y_f}\}$.

Then, we can see that the following relationships hold:

$$\frac{\beta_\theta + \gamma_\theta}{\alpha}(t_\theta) = \frac{\beta_\theta - \gamma_\theta}{\alpha}(t_\theta) > 0, \tag{3.65}$$

$$\lim_{t \to 2\pi-} \frac{\beta_\theta + \gamma_\theta}{\alpha}(t) = \infty, \tag{3.66}$$

$$\frac{\beta_\theta - \gamma_\theta}{\alpha}(T_d) = 0. \tag{3.67}$$

The function $(\beta_\theta + \gamma_\theta)/\alpha$ is continuous with respect to t in $[t_\theta, 2\pi)$, also $(\beta_\theta - \gamma_\theta)/\alpha$ is continuous in $[t_\theta, T_d]$. Therefore, by the intermediate value theorem, for almost all pairs of $\{\boldsymbol{x_f}, \boldsymbol{y_f}\}$, there exist at least one $t \in (0, T_d]$ which satisfies (3.62) be zero. This root is the t_f we want to obtain. Such t_f can be obtained numerically, e.g., by applying the bisection method to (3.62).

Once t_f is determined, r, h and $\boldsymbol{\Omega}$ can be obtained by just substituting t_f into (3.58), (3.59) and (3.46) sequentially as Fig. 3.3. In summary, we have shown that there exists a helix
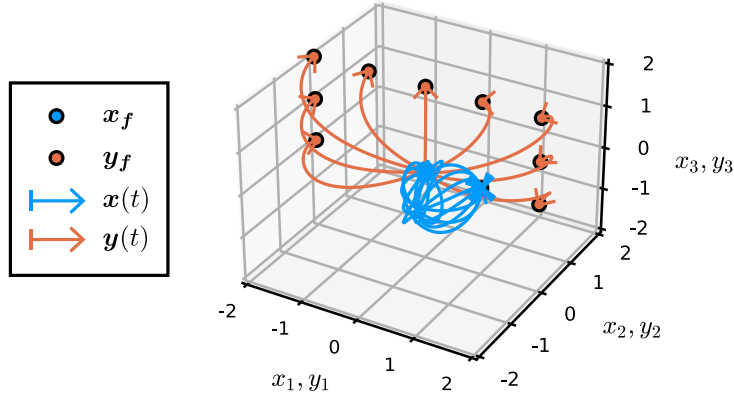
Fig. 3.4 By a helix path on the $\boldsymbol{x}$, six-dimensional states $\boldsymbol{x}(t), \boldsymbol{y}(t)$ are steered optimally to any given target point.

path reaching almost any target point and also show the method to find such a path with the smallest phase angle.

Remark 1 (Excepted cases: $\boldsymbol{x_f}^\top \cdot \boldsymbol{y_f} = 0$, $\boldsymbol{x_f} \times \boldsymbol{y_f} = \boldsymbol{0}$). *Although we have provided a path determination method for almost all target points, the above procedure cannot be used to find a solution path for the regions of measure zero such that the parallel or orthogonal conditions are satisfied. For such cases, the solution path will be obtained by appropriate case method. For the orthogonal case $\boldsymbol{x_f}^\top \cdot \boldsymbol{y_f} = 0$, we should degenerate the system into the 2-inputs 3-states system. For the parallel case $\boldsymbol{x_f} \times \boldsymbol{y_f} = \boldsymbol{0}$, there exist numerous optimal $\boldsymbol{\Omega}$ due to rotational symmetry, and one of them can be chosen as an optimal path's parameter.*

3.5 Numerical experiments

In this section, we show some numerical examples. We first discuss generic examples, then focus on four extreme cases. In the figures, the given target points $\boldsymbol{x_f}, \boldsymbol{y_f}$ are plotted as dots, and the numerically obtained paths $\boldsymbol{x}(t), \boldsymbol{y}(t)$ are plotted as lines. Note that the state dimension of the whole system is six, but we divide it into the base coordinates $\boldsymbol{x}$ and the fiber coordinates $\boldsymbol{y}$ in order to overlay them as a trajectory on a three-dimensional space.

3.5.1 Generic optimal paths and their accuracy

First, we state that the numerical solutions are obtained for a set of comprehensive target points with reasonable errors. Symmetry on $\mathbb{SO}(3)$ is not covered. In addition, base coordinates $\boldsymbol{x}$ is also normalized. Based on these considerations, we set the target values in the range of

$$\boldsymbol{x_f} = \begin{bmatrix} 1.0 & 0.0 & 0.0 \end{bmatrix}^\top, \tag{3.68}$$

$$\boldsymbol{y_f} = \begin{bmatrix} y_{f1} & 0.0 & y_{f3} \end{bmatrix}^\top, \tag{3.69}$$

$$y_{f1} \in [-100.0, 100.0], \quad y_{f3} \in [0.0, 100.0]. \tag{3.70}$$

Fig. 3.5 Helix path: even if $\boldsymbol{x_f} \times \boldsymbol{y_f} \simeq 0$, we can find out the optimal path. $\boldsymbol{y}(t)$ is steered to $\boldsymbol{y_f}$ by the helix path on the $\boldsymbol{x}$.

We cut the mesh at 0.1 intervals, and exclude the case $|\boldsymbol{y_f}| = 0.0$ or $\theta = 0.0$. The termination error μ was evaluated by

$$\mu := \max \left\{ \frac{|\boldsymbol{x_p} - \boldsymbol{x_f}|}{|\boldsymbol{x_f}|}, \frac{|\boldsymbol{y_p} - \boldsymbol{y_f}|}{|\boldsymbol{y_f}|} \right\}, \tag{3.71}$$

where $\boldsymbol{x_p}, \boldsymbol{y_p}$ denote the termination point which calculated by the set of numerically obtained parameters $\{r, h, t_f, \boldsymbol{\Omega}\}$. As a result of the above settings, numerical solutions were obtained for all cases, and the termination error μ was less than 0.02. Figure 3.4 shows several sampled paths which steer six-dimensional states $\boldsymbol{x}(t), \boldsymbol{y}(t)$ optimally. Introducing the helix path representation on $\boldsymbol{x}$ enabled us to gain the optimal paths on the six-dimensional underactuated system quasi-analytically.

3.5.2 Extreme case 1: A typical optimal helix path

Figure 3.5 shows the first extreme case where $\boldsymbol{x_f}$ and $\boldsymbol{y_f}$ are almost parallel, which yields a typical path of this study. We set the target point as $\boldsymbol{x_f} = [2.0\ 0.0\ 0.0]^\mathsf{T}$, $\boldsymbol{y_f} = [-1.0\ 0.0\ 0.01]^\mathsf{T}$. Even in this case, the optimal path is obtained, and the obtained parameters are $\{r, h, t_f\} \simeq \{0.351, -0.224, 8.49\}$.

3.5.3 Extreme cases 2–4: Encompassing relationship with the known shortest paths

The remaining three cases correspond to cases for which the global optimal paths are already known in previous studies. We show that the paths of this study encompass the global optimal paths on these three cases. The two-input three-state Brockett's canonical system can be represented as a special case of the three-input six-state Brockett's canonical system; where the case of $\boldsymbol{x}^\mathsf{T} \cdot \boldsymbol{y} = 0$, $\boldsymbol{x}, \boldsymbol{y} \in \mathbb{R}^3$ are satisfied. Therefore, we show the three cases where $\boldsymbol{x}$ is embedded in the horizontal plane and $\boldsymbol{y}$ is embedded in the vertical axis.

Figure 3.6 and Fig. 3.7 show the cases where $\boldsymbol{x}(t)$ traces a circle and an arc, respectively. For the case of the circle, the target point is $\boldsymbol{x_f} = [0.01\ 0.0\ 0.0]^\mathsf{T}$, $\boldsymbol{y_f} = [0.01\ 0.0\ 2.0]^\mathsf{T}$, and the obtained parameters are $\{r, h, t_f\} \simeq \{0.564, 0.00, 6.27\}$. For the case of the arc, the target point is $\boldsymbol{x_f} = [1.0\ 0.0\ 0.0]^\mathsf{T}$, $\boldsymbol{y_f} = [0.01\ 0.0\ 2.0]^\mathsf{T}$, and the obtained parameters are
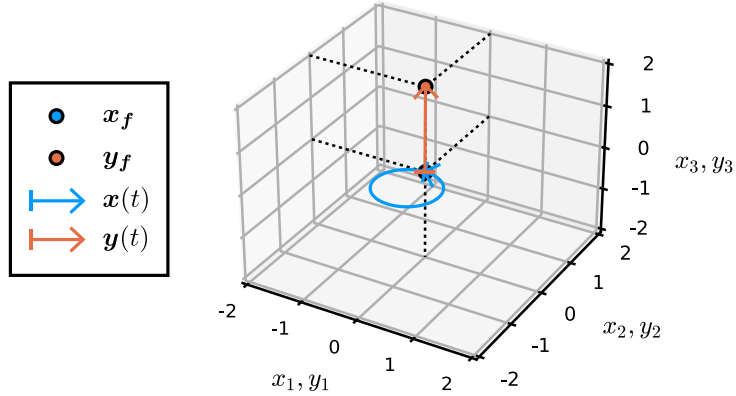
Fig. 3.6 Circular path: $\boldsymbol{y}(t)$ moves in the vertical direction, while $\boldsymbol{x}(t)$ moves along the circular path in the horizontal plane.
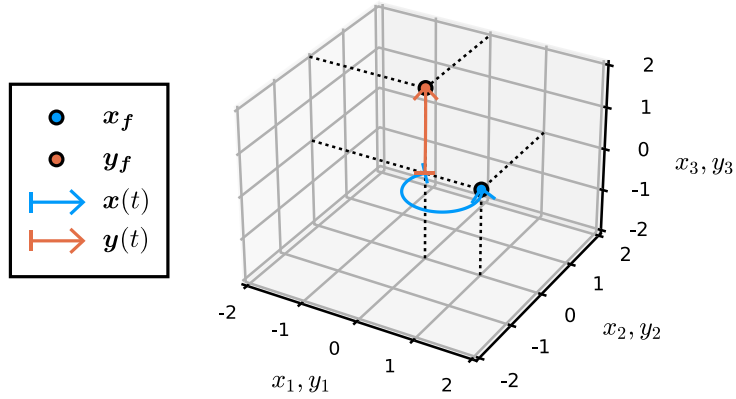
Fig. 3.7 Arc path: $\boldsymbol{y}(t)$ moves in the vertical direction, while $\boldsymbol{x}(t)$ moves along the arc path in the horizontal plane.

$\{r, h, t_f\} \simeq \{0.613, 0.00274, 4.38\}$. In both cases, the pitch of helix $h \simeq 0$, and in the case of the circle, the phase angle $t_f \simeq 2\pi$. These paths are consistent with the known shortest paths.

Figure 3.8 shows the case where $\boldsymbol{x}(t)$ traces a straight path. The target point is $\boldsymbol{x_f} = [1.0 \ 0.0 \ 0.0]^{\mathsf{T}}$, $\boldsymbol{y_f} = [0.001 \ 0.0 \ 0.01]^{\mathsf{T}}$, and the obtained parameters are $\{r, h, t_f\} \simeq \{0.0109, 0.125, 8.01\}$. This path is also consistent with the known optimal paths. We note that there are two ways to represent a straight-like path by the helix paths (3.37), one is $\{rt = |\boldsymbol{x_f}|, \ h \simeq 0, \ t_f \simeq 0\}$ and the other one is $\{ht = |\boldsymbol{x_f}|, \ r \simeq 0\}$, and the numerical solutions vary significantly depending on the angle θ.

3.6 Conclusion

In this chapter, I have presented a *helix path representation* as the optimal paths on the three-input six-dimensional canonical system. Specifically, on Brockett's local canonical system, we have shown that the local optimal paths are parameterized as the helix paths. Then a
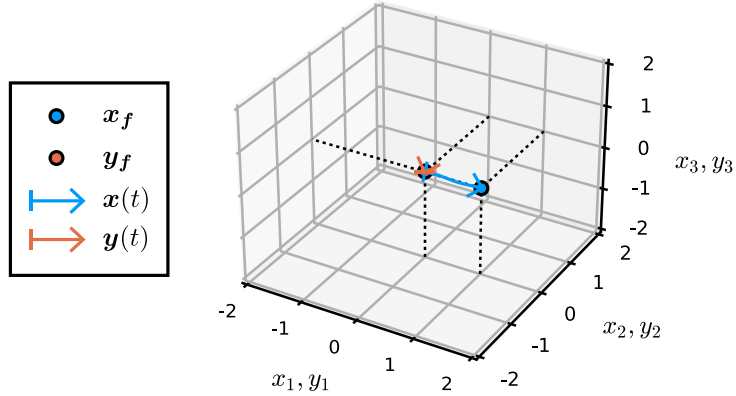
Fig. 3.8   Straight path: the straight path on the $\boldsymbol{x}$ does not generate the displacement of $\boldsymbol{y}(t)$.

procedure to determine the helix path that reaches any given target point was presented. The helix paths encompass the global optimal paths for the two-inputs three-dimensional canonical system, which is visually demonstrated. The followings are key results of this chapter.

- The parametric representation of the optimal paths was obtained as an explicit function $\boldsymbol{x}(t) = \boldsymbol{\Omega} \cdot \boldsymbol{\xi}_{r,h}(t)$.
- The parameters of helix r, h, t_f and $\boldsymbol{\Omega}$ are geometrically distinct (representing the radius, pitch, phase angle, and orientation, respectively).

Future work includes the following topics. As indicated by the Brockett's necessary condition[28], the resulting path would depend discontinuously on the choice of target points, around the points of exception in the boundary condition (3.47). In addition, the consideration of this study is local in two meanings. One is that the target system is only a local canonical system, and it is desirable to link it to Lie group representations or more general forms. The other is that the optimality of the paths is local in the sense of only satisfying the stationary conditions, and this analysis is an interesting problem in the future.

Chapter 4

A Kinematic-Dual Snake Robot: Undulatory Mobile Robot Driven by Controllable Side-Thrust Links

4.1 Introduction of the kinematic-dual snake

The snake robots are kinematically interesting mobile mechanisms in which postural deformation produces positional translation. Mechanical analysis of a living snake was performed in the 1940s [29]. The original snake robot was introduced by Hirose [30, 31]. The original robotic model mimics a living snake, as shown in Fig. 4.1(a): scales on the snake's belly, which prevent lateral slippage, are modeled by passive wheels, and its musculature is modeled by active joints. The passive wheels, which prevent the links from moving in the lateral directions, are formulated as $\dot{x}_i \sin \theta_i - \dot{y}_i \cos \theta_i = 0$, and the active joints are formulated as $\dot{\theta}_{i+1} - \dot{\theta}_i = \omega_i$.

Here we present control-theoretical studies for the original snake with kinematic assumptions: fixed passive wheels, no side-slippage, and no frictional losses. Head position control based on the dynamics model has been proposed in [32, 33, 34, 35]. For the kinematic models, control of the entire state quantities (i.e., $n + 2$ degrees of freedom in the case of n-link) has been studied as an example of the nonlinear control theory based on the differential geometry [5, 36]. Ostrowski [37] achieved a general method for controlling undulatory locomotion, whereby internal changes in shape generate motions. Ishikawa [38, 39] applied this method to the original snake and described its nonlinear controllability and control strategy. The considerations in the above studies have shown that it is complicated to control the shape of the original snakes.

The original snake has the advantage provided by distributive traction, but its capability of motion is limited. Therefore, string-like mobile mechanisms inspired by the original snake have been developed. Studies that are relatively close to the original snake are those that assume anisotropic groud friction property instead of nonholonomic constraint [40] and those that lift or eliminate some wheels [41, 42, 43, 44]. Other examples include the worm-like robots that assume isotropic ground friction [45, 46], and the robots focused on traversing rough terrain with active wheels as well as joints [47, 48, 49, 50, 51, 52]. We approached this development of the string-like mobile mechanisms by focusing on the kinematics and control structure.

Now let us consider a *mechanical-dual* snake as the first step toward introducing a *kinematic-dual* snake, which the authors previously presented in [53, 54, 55]. The original snake consists of side-slip-constraint wheels and active joints; the active joints are used as input. The side-slip constraint used in the original snake can be treated as a special case of a *side-thrust input*.

Step 1: reversing the mechanism

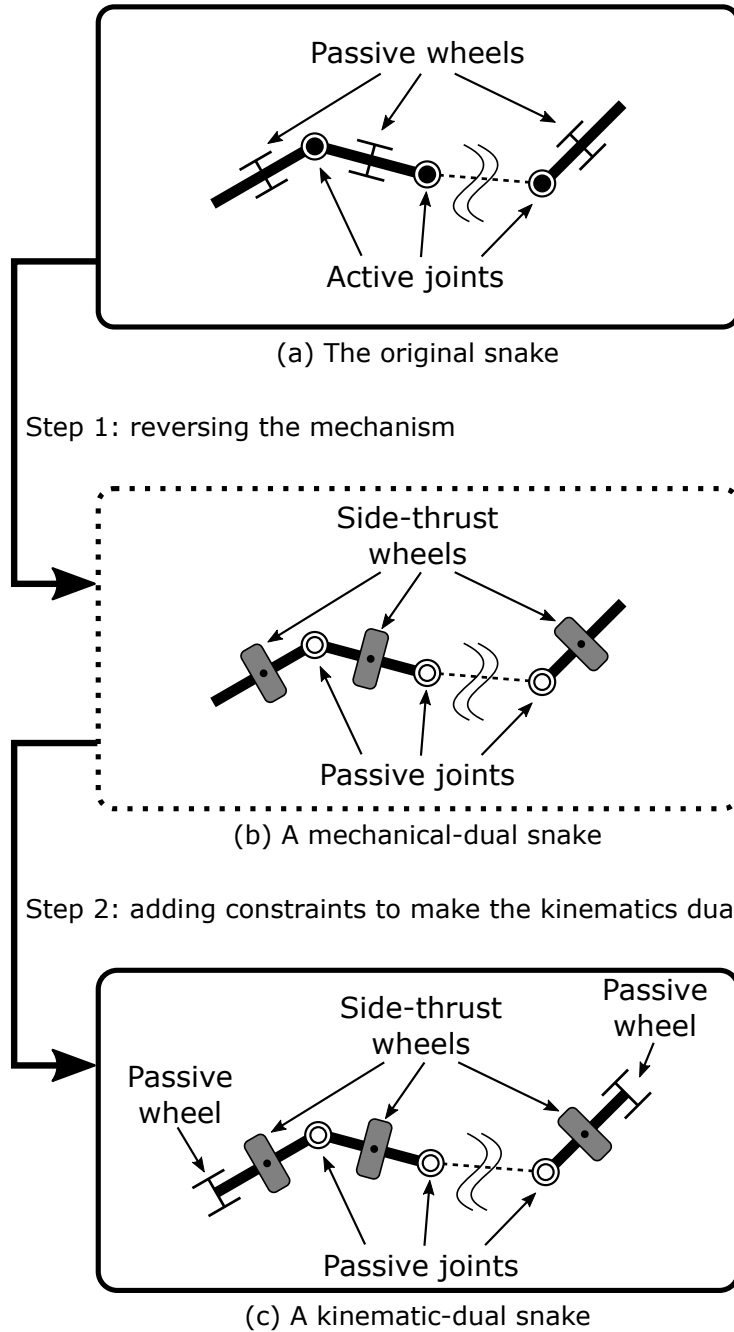Step 2: adding constraints to make the kinematics dual

Fig. 4.1 (a): Subfigure shows the original snake. (b): Reversing the mechanism of the original snake to use the wheels as input results in a mechanical-dual snake. This is not well-defined kinematically because the number of degrees of freedom exceeds its constraints. (c): Therefore, we add two kinematic constraints, creating the proposed kinematic-dual snake .
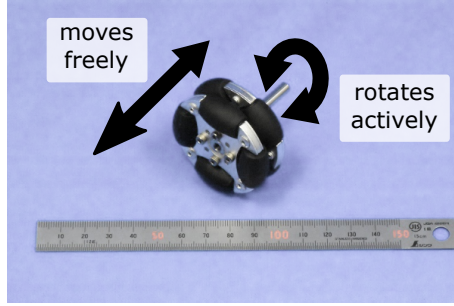
Fig. 4.2 The omnidirectional wheel is composed of a parent wheel and child wheels attached to it. In the proposed snake described in this chapter, only the parent wheel is used in active rotation.

That is, $\dot{x}_i \sin\theta_i - \dot{y}_i \cos\theta_i = 0$ is a special case of $\dot{x}_i \sin\theta_i - \dot{y}_i \cos\theta_i = v_i$ with constant zero input $v_i = 0$. By considering this notion, we conceived of a mechanism that uses the side-thrust velocities as inputs, a mechanism dual to the original snake, as shown in Fig. 4.1(b). The side-thrust input could be implemented by attaching an omnidirectional wheel (Fig. 4.2) that can rotate actively in the lateral direction of the link.

The original snake and the mechanical-dual snake have a reverse relationship in the mechanical sense; however, their kinematics are not in a dual relation. Therefore, as the second step, we refine the mechanical-dual snake to create a system whose kinematic model is dual to the original snake's; we propose this model as a kinematic-dual snake. It is derived as follows.

The kinematic equations for the original snake can be written in the following form:

$$\boldsymbol{D}(\boldsymbol{\xi}) \cdot \dot{\boldsymbol{\xi}} = \begin{bmatrix} 0 \\ \vdots \\ 0 \end{bmatrix}, \quad \boldsymbol{A}(\boldsymbol{\xi}) \cdot \dot{\boldsymbol{\xi}} = \begin{bmatrix} u_1 \\ u_2 \end{bmatrix} \tag{4.1}$$

where $\boldsymbol{\xi} \in \mathbb{R}^{n+2}$ denotes the state of the system, and u_1, u_2 denote the control input. The left-hand side of the equations indicates the side-slip constraints imposed by the passive wheels, and the right-hand side of the equations indicates the inputs for the remaining degrees of freedom.

The kinematic equations for the mechanical-dual snake, on the other hand, are not well defined because the total number of inputs and constraints is less than the number of degrees of freedom. Thus, we add two kinematic constraints to the mechanical-dual snake. As the kinematic constraints can be chosen arbitrarily, for reasons of symmetry, we choose to add a side-slip constraint at each end of the mechanical-dual snake, as shown in Fig. 4.1-(c). With this addition, the kinematic model is now well defined and is written as follows:

$$\boldsymbol{D}(\boldsymbol{\xi}) \cdot \dot{\boldsymbol{\xi}} = \begin{bmatrix} u_1 \\ \vdots \\ u_n \end{bmatrix}, \quad \boldsymbol{A}(\boldsymbol{\xi}) \cdot \dot{\boldsymbol{\xi}} = \begin{bmatrix} 0 \\ 0 \end{bmatrix} \tag{4.2}$$

The left-hand side of the equations indicates the side-thrust control inputs, which are implemented by the active omnidirectional wheels, and the right-hand side of the equations indicates the two constraints implemented by the passive wheels at both ends of the robot. Equations (4.1) and (4.2) have a dual relationship with each other. Thus, we propose the mechanism shown in Fig. 4.1-(c) as a *kinematic-dual snake robot*, whose kinematic model is dual to the
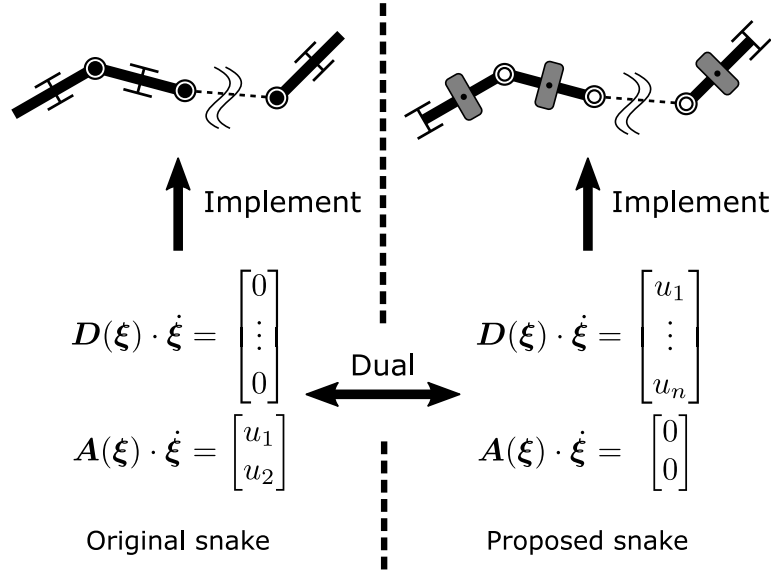
Fig. 4.3 Dual kinematic models and their implementations. The two kinematic models are dual to each other and can be implemented as mechanical systems.

original snake robot. Fig. 4.3 shows the relationship between the two snake robots in terms of their kinematics and mechanisms.

In this chapter, we address the following topics. In Section 4.1, we have introduced a mechanism whose kinematic model is dual to that of the original snake. In Section 4.2, we derive kinematic models for the two snake robots and demonstrate that they are dual to each other. In Section 4.3, the nonlinear controllability of the kinematic-dual snake is proved for the three-link case, and a simple motion planning method is presented. In Section 4.4, we derive the dynamics of the proposed mechanism, and feasible motions are shown. Finally, in Section 4.5, we demonstrate the motions of an actual robot based on the motion planning in Section 4.4.

4.2 Duality of the kinematic equations

In this section, we explain how the kinematic equations of the original snake and the proposed snake are dual to each other.

4.2.1 Definitions and assumptions

The respective mechanical structures of the two snake robots are shown in Fig. 4.1(a) and (c). The robots are composed of n links in series connected by active joints in the original snake and passive joints in the proposed snake. At the center of each link in the original snake and the proposed snake is an ordinary wheel or an active omnidirectional wheel, respectively. The proposed snake has ordinary passive wheels at both ends.

The configuration variables are defined as shown in Fig. 4.4. We refer to one end segment as the first link and the other end segment as the nth link. (In the figure, $n = 3$.) The positions of the two ends are defined as (x_F, y_F) and (x_R, y_R), respectively. For each link, (x_i, y_i) and θ_i $(i = 1, 2, \ldots, n)$ represent its center position, and its counter-clockwise angle

Fig. 4.4   Definition of configuration variables for the both three-link snakes

relative to the x-axis, respectively. v_i represents the side-thrust velocity of the corresponding omnidirectional wheel. ω_i represents the angular velocity of the corresponding joints. The unit length is defined as half the length of a link.

In order to derive the kinematic models, we adopt the following assumptions.

- *Planar motion:* only planar motion is considered.
- *Non-slip condition:* the wheels (including the omnidirectional wheels as well as the ordinary wheels) do not slip in the link's lateral directions.
- *Mechanical limit on joints:* joint angles are mechanically limited to the range $(-\pi/2, \pi/2)$.

4.2.2   Derivations

First, we derive the kinematic equations for the proposed snake. The velocities of the center of the ith link and the rear endpoint are respectively represented by

$$
\dot{x}_i = \dot{x}_F - 2\sum_{j=1}^{i-1} \dot{\theta}_j \sin\theta_j - \dot{\theta}_i \sin\theta_i
$$

$$
\dot{y}_i = \dot{y}_F + 2\sum_{j=1}^{i-1} \dot{\theta}_j \cos\theta_j + \dot{\theta}_i \cos\theta_i
$$

(4.3)

and

$$
\dot{x}_R = \dot{x}_F - 2\sum_{j=1}^{i-1} \dot{\theta}_j \sin\theta_j
$$

$$
\dot{y}_R = \dot{y}_F + 2\sum_{j=1}^{i-1} \dot{\theta}_j \cos\theta_j
$$

(4.4)

The lateral velocity of the ith link is represented by

$$
-\dot{x}_i \sin\theta_i + \dot{y}_i \cos\theta_i = v_i
$$

(4.5)

Similarly, the non-slip assumption for the ordinary wheels is expressed by

$$-\dot{x}_F \sin\theta_1 + \dot{y}_F \cos\theta_1 = 0$$
$$-\dot{x}_R \sin\theta_n + \dot{y}_R \cos\theta_n = 0 \tag{4.6}$$

By combining (4.3), (4.4), (4.5), and (4.6), we obtain the following kinematic equations in the same form as that of (4.2)

$$\boldsymbol{D}(\boldsymbol{\xi_n}) \cdot \dot{\boldsymbol{\xi}}_n = \begin{bmatrix} v_1 \\ \vdots \\ v_n \end{bmatrix}, \quad \boldsymbol{A}(\boldsymbol{\xi_n}) \cdot \dot{\boldsymbol{\xi}}_n = \begin{bmatrix} 0 \\ 0 \end{bmatrix} \tag{4.7}$$

where $\boldsymbol{\xi_n} := \begin{bmatrix} \theta_1 & \theta_2 & \cdots & \theta_n & x_F & y_F \end{bmatrix}^T$.

The matrix $[\boldsymbol{D}(\boldsymbol{\xi_n}) \ \boldsymbol{A}(\boldsymbol{\xi_n})]^T$ is nonsingular almost everywhere, and in this case, an arbitrary choice for $\boldsymbol{v} := [v_1 \ \cdots \ v_n]^T \in \mathbb{R}^n$ can be used as inputs that are independent of each other.

The joint constraints of the original snake are given by (4.3) and (4.4) as the same as those for the proposed snake. Each link has an ordinary wheel that does not slip sideways, and so the lateral velocity of the ith link is given by

$$-\dot{x}_i \sin\theta_i + \dot{y}_i \cos\theta_i = 0 \tag{4.8}$$

The angular velocity of the ith joint is represented by

$$\dot{\theta}_{i+1} - \dot{\theta}_i = \omega_i \tag{4.9}$$

By combining (4.3), (4.4), (4.8), and (4.9), we obtain the following kinematic equations:

$$\boldsymbol{D}(\boldsymbol{\xi_n}) \cdot \dot{\boldsymbol{\xi}}_n = \begin{bmatrix} 0 \\ \vdots \\ 0 \end{bmatrix}, \quad \boldsymbol{A}'(\boldsymbol{\xi_n}) \cdot \dot{\boldsymbol{\xi}}_n = \begin{bmatrix} \omega_1 \\ \vdots \\ \omega_{n-1} \end{bmatrix} \tag{4.10}$$

Because the equations in (4.10) are $(2n-1)$-dimensional equations for a system with $n+2$ degrees of freedom, we cannot determine the ω_i values independently from each other; that is, there is no state change $\dot{\boldsymbol{\xi}}_n$ that satisfies (4.10) for values of ω_i that are determined independently from each other. Forcing an independently determined ω_i on an actual mechanical system will cause the wheels to slip sideways.

The existence condition for a $\dot{\boldsymbol{\xi}}_n$ satisfying (4.10) is that $\boldsymbol{\omega} := [\omega_1 \ \cdots \ \omega_{n-1}]^T \in \mathbb{R}^{n-1}$ be representable in the following form (because the remaining degrees of freedom are 2):

$$\boldsymbol{\omega} = \boldsymbol{A}''(\boldsymbol{\xi_n}) \cdot \boldsymbol{u} \tag{4.11}$$

where $\boldsymbol{u} := [u_1 \ u_2]^T$ represents the arbitrary generalized velocities of the system, and matrix $\boldsymbol{A}''(\boldsymbol{\xi_n})$ is a coordinate transformation matrix from $\boldsymbol{u}$ to $\boldsymbol{\omega}$.

Bearing in mind the proposed snake, we define the arbitrary $\boldsymbol{u}$ as the lateral velocities of both ends of the robot. Then, the kinematic equations of the original snake are expressed in terms of constraints and inputs independent of each other, using matrices $\boldsymbol{D}(\boldsymbol{\xi_n})$ and $\boldsymbol{A}(\boldsymbol{\xi_n})$, as follows:

$$\boldsymbol{D}(\boldsymbol{\xi_n}) \cdot \dot{\boldsymbol{\xi}}_n = \begin{bmatrix} 0 \\ \vdots \\ 0 \end{bmatrix}, \quad \boldsymbol{A}(\boldsymbol{\xi_n}) \cdot \dot{\boldsymbol{\xi}}_n = \begin{bmatrix} u_1 \\ u_2 \end{bmatrix} \tag{4.12}$$

Equations (4.7) and (4.12) are dual to each other, and therefore the proposed snake is dual to the original snake.

4.3 Lie bracket motion based on kinematic controllability

The minimum number of links for which the proposed mechanism is first-order nonlinearly controllable is three; thus, we discuss the three-link model in more detail.

4.3.1 State equation for the three-link system

To analyze the nonlinear controllability of the three-link model, we formulate (4.7) in the state equation form. We define the state vector $\boldsymbol{\xi}$ and the input $\boldsymbol{v}$ as follows:

$$\boldsymbol{\phi} := \begin{bmatrix} \phi_1 \\ \phi_3 \end{bmatrix} := \begin{bmatrix} \theta_1 - \theta_2 \\ \theta_3 - \theta_2 \end{bmatrix}, \quad \boldsymbol{\xi} := \begin{bmatrix} \boldsymbol{\phi} \\ x_2 \\ \theta_2 \\ y_2 \end{bmatrix}, \quad \boldsymbol{v} := \begin{bmatrix} v_1 \\ v_2 \\ v_3 \end{bmatrix} \tag{4.13}$$

Using $\boldsymbol{\xi}$, $\boldsymbol{v}$, and the rotation matrix $\boldsymbol{R_{\theta_2}}$, the three-link kinematic equation is obtained as

$$\boldsymbol{A}(\boldsymbol{\phi})\boldsymbol{R_{\theta_2}^{-1}}\dot{\boldsymbol{\xi}} = \begin{bmatrix} \boldsymbol{v} \\ 0 \\ 0 \end{bmatrix} \tag{4.14}$$

where $\boldsymbol{A}(\boldsymbol{\phi}) \in \mathbb{R}^{5\times 5}$. The determinants of $\boldsymbol{A}(\boldsymbol{\phi})$ and $\boldsymbol{A_{\lambda 2}}(\boldsymbol{\phi})$ are the followings:

$$\det \boldsymbol{A}(\boldsymbol{\phi}) = \sin(\phi_1 + \phi_3) \tag{4.15}$$
$$\det \boldsymbol{A_{\lambda 2}}(\boldsymbol{\phi}) = \cos\phi_1 + \cos\phi_3 + \cos\phi_1 \cos\phi_3 \tag{4.16}$$

Since $|\phi_1(t)| < \pi/2$ and $|\phi_3(t)| < \pi/2$ hold for all t by the mechanical limit assumption, $\boldsymbol{A_{\lambda 2}}(\boldsymbol{\phi})$ is nonsingular everywhere.

If $\boldsymbol{A}(\boldsymbol{\phi})$ is nonsingular; the state equation is obtained in the following symmetric affine form:

$$\dot{\boldsymbol{\xi}} = \boldsymbol{R_{\theta_2}}\boldsymbol{A}(\boldsymbol{\phi})^{-1} \begin{bmatrix} \boldsymbol{v} \\ 0 \\ 0 \end{bmatrix} \tag{4.17}$$

$$= \boldsymbol{R_{\theta_2}} \begin{bmatrix} \boldsymbol{I} \\ \boldsymbol{S}(\boldsymbol{\phi}) \end{bmatrix} (\boldsymbol{A_1}(\boldsymbol{\phi}) + \boldsymbol{A_2}(\boldsymbol{\phi})\boldsymbol{S}(\boldsymbol{\phi}))^{-1}\boldsymbol{v} \tag{4.18}$$

where

$$\boldsymbol{S}(\boldsymbol{\phi}) := -\boldsymbol{A_{\lambda 2}}(\boldsymbol{\phi})^{-1}\boldsymbol{A_{\lambda 1}}(\boldsymbol{\phi}) \tag{4.19}$$

We can equivalently write it in the following form:

$$\dot{\boldsymbol{\xi}} = \begin{bmatrix} \boldsymbol{g_1}(\boldsymbol{\xi}) & \boldsymbol{g_2}(\boldsymbol{\xi}) & \boldsymbol{g_3}(\boldsymbol{\xi}) \end{bmatrix} \boldsymbol{v} \tag{4.20}$$

4.3.2 Controllability of the kinematic-dual snake

Let us now check the nonlinear controllability of the kinematic-dual snake. The state equation describing the kinematics is written as (4.20). The span of $\boldsymbol{g_i}$ and its first-order Lie brackets are full row rank except for the singular posture. Therefore, state $\boldsymbol{\xi}$ is nonlinearly controllable by using $\boldsymbol{v}$ as input.
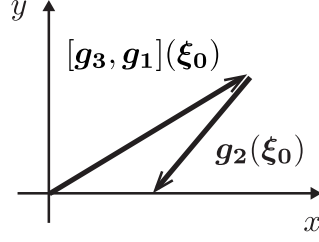
Fig. 4.5 Combining $[\boldsymbol{g_3}, \boldsymbol{g_1}](\boldsymbol{\xi_0})$ and $\boldsymbol{g_2}(\boldsymbol{\xi_0})$ with appropriate weights produces a net motion in the x-direction.

4.3.3 Lie bracket based motion planning

We demonstrate a simple approach for archiving the desired displacement based on the non-linear controllability analysis. As an example, we describe a case in which the system moves only in the x-direction.

Let initial state $\boldsymbol{\xi_0} = \begin{bmatrix} \pi/4 & \pi/4 & 0 & 0 & 0 \end{bmatrix}^T$. Then the two vectors $[\boldsymbol{g_3}, \boldsymbol{g_1}](\boldsymbol{\xi_0})$ and $\boldsymbol{g_2}(\boldsymbol{\xi_0})$ are written as follows:

$$[\boldsymbol{g_3}, \boldsymbol{g_1}](\boldsymbol{\xi_0}) = \begin{bmatrix} 0 \\ 0 \\ -4 - 2\sqrt{2} \\ 0 \\ -4 \end{bmatrix}, \quad \boldsymbol{g_2}(\boldsymbol{\xi_0}) = \begin{bmatrix} 0 \\ 0 \\ 1 \\ 0 \\ 1 \end{bmatrix} \tag{4.21}$$

The two vectors $[\boldsymbol{g_3}, \boldsymbol{g_1}](\boldsymbol{\xi_0})$ and $\boldsymbol{g_2}(\boldsymbol{\xi_0})$ operate only on x and y, and these two vectors are linearly independent of each other. Therefore, we can make arbitrary vectors of (x_2, y_2) by combining $[\boldsymbol{g_3}, \boldsymbol{g_1}](\boldsymbol{\xi_0})$ and $\boldsymbol{g_2}(\boldsymbol{\xi_0})$ with appropriate weights. For example, the following linear combination indicates a pure x-axis vector, as shown in Fig. 4.5:

$$-\frac{1}{2\sqrt{2}}[\boldsymbol{g_3}, \boldsymbol{g_1}](\boldsymbol{\xi_0}) - \sqrt{2}\boldsymbol{g_2}(\boldsymbol{\xi_0})$$

$$= \begin{bmatrix} 0 \\ 0 \\ 1 + \sqrt{2} \\ 0 \\ \sqrt{2} \end{bmatrix} + \begin{bmatrix} 0 \\ 0 \\ -\sqrt{2} \\ 0 \\ -\sqrt{2} \end{bmatrix} = \begin{bmatrix} 0 \\ 0 \\ 1 \\ 0 \\ 0 \end{bmatrix} \tag{4.22}$$

To implement the motion that corresponds to (4.22), we apply the time sequence of inputs shown in Fig. 4.6. The input for the time from $t = 0$ to $t = 6$ generates the displacement $[\boldsymbol{g_3}, \boldsymbol{g_1}](\boldsymbol{\xi_0})$, and the input for the time from $t = 6$ to $t = 7$ generates the displacement $\boldsymbol{g_2}(\boldsymbol{\xi_0})$.

Fig. 4.7 shows the results of a numerical simulation. The two subfigures show the time sequences of shape and orientation and the position, respectively. Fig. 4.8 displays the top-view sequential depictions of the robot, showing its motion. As a result of the motion, only x has changed; the other state values have not.

The state value y changes slightly as a result of the numerical motion. This is because (2.4) uses an approximation for the small value ϵ. Whereas the approximation error increases as ϵ
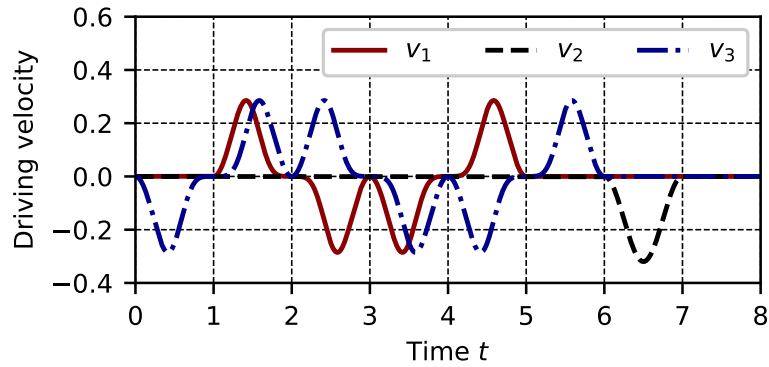
Fig. 4.6   This time sequence of inputs moves the state in the x-direction.
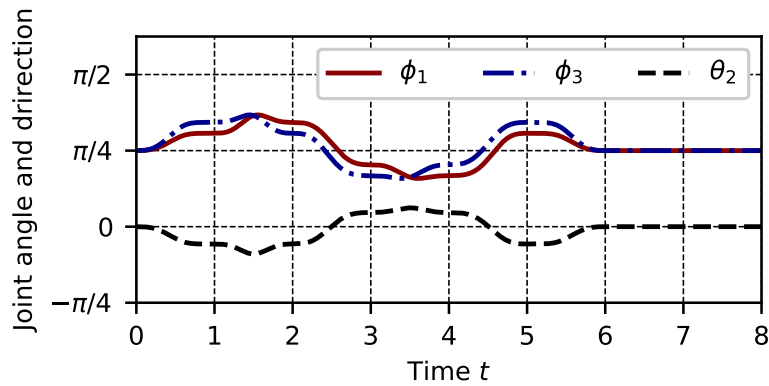
(a) Time sequence of the joint angles ϕ_1, ϕ_3 and the orientation of the second link θ_2: none of the angles have changed from its original value.
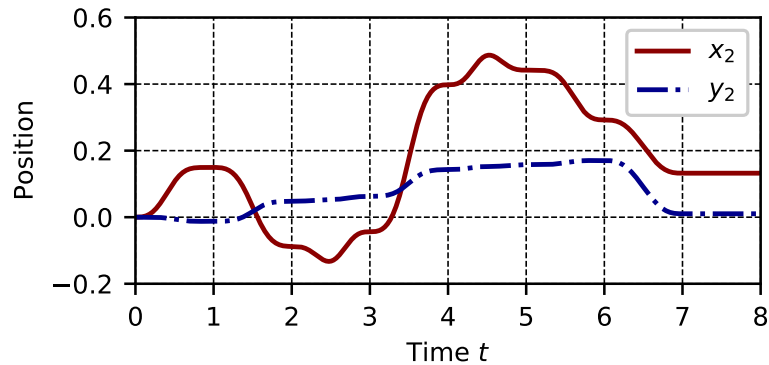
(b) Time sequence of the robot's position: as a result of the motion, only the x value has changed.

Fig. 4.7   Time sequence of the controlled translation: only x has changed.
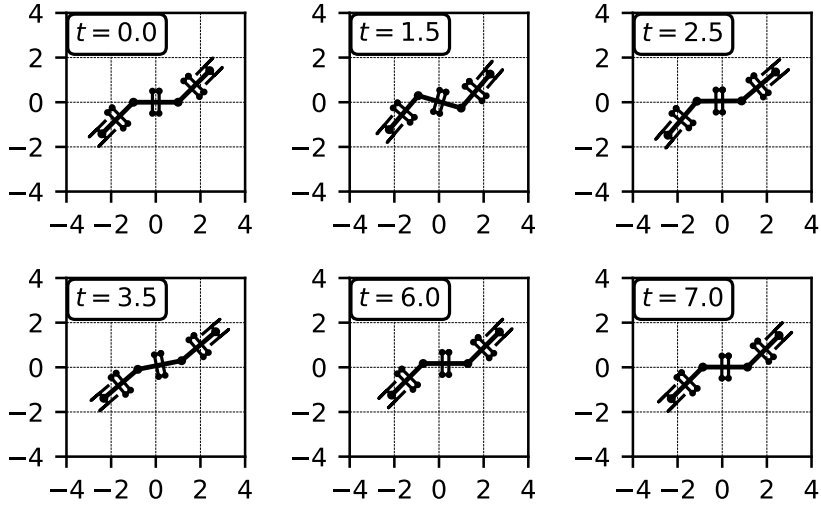
Fig. 4.8 The figures show the controlled translation: changing the position without changing the shape or the orientation.
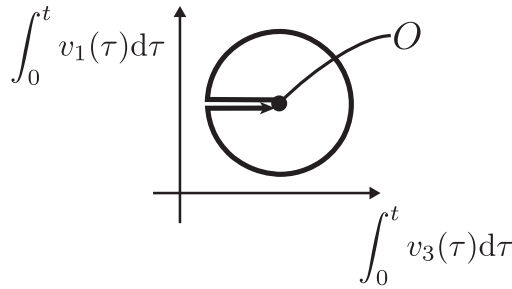
Fig. 4.9 In order to reduce the approximation error, we apply the input that traces a circular path as close to the origin O as possible.

increases, the Lie bracket motion uses changes in the tangent space to represent state changes. Thus, there is a dilemma: as the change in state decreases, the amount of movement likewise decreases.

We can reduce the approximation error by setting up the input path using several techniques. For example, the time integration of the input in Fig. 4.6 follows the path shown in Fig. 4.9. The path remains as close to the origin $\boldsymbol{\xi_0}$ as possible while maximizing the the closed-loop area.

4.4   Skating motion without avoiding the singular posture

The control approach proposed in the previous section is based on a drift-free nonlinear system that corresponds to the kinematic equation. Although this approach is easily understood, it must avoid the singular posture. Thus, we design undulation motions, called dynamic skating, to include the singular posture.

To design the skating motion, we first derive the dynamics. Next, we describe the method for determining the motion and the motion constraints. Finally, we give a numerical example.

4.4.1 Dynamics of the kinematic-dual snake

In this derivation, we do not consider losses from friction. Let m be the mass of a link, which is defined as the unit mass, and let J be the vertical moment of inertia of the link. (Other masses and moments of inertia are not considered in this chapter.) We define force vectors as follows:

$$\boldsymbol{f} := \begin{bmatrix} f_1 & f_2 & f_3 \end{bmatrix}^T, \quad \boldsymbol{f_\lambda} := \begin{bmatrix} f_F & f_R \end{bmatrix}^T \tag{4.23}$$

where f_i denotes the driving forces of the ith omnidirectional wheel, and f_F and f_R denote the constraint forces of the respective end wheels.

We then begin to derive the equations of motion based on the method described in [27]. By the virtual work principle, the following equation for the virtual work holds for all $\boldsymbol{v}$, $\boldsymbol{f}$, and $\boldsymbol{f_\lambda}$:

$$\delta W = \dot{\boldsymbol{\xi}}^T \cdot \boldsymbol{f_\xi} = \begin{bmatrix} \boldsymbol{v} \\ 0 \\ 0 \end{bmatrix}^T \begin{bmatrix} \boldsymbol{f} \\ \boldsymbol{f_\lambda} \end{bmatrix} \tag{4.24}$$

where $\boldsymbol{f_\xi}$ denotes the generalized force using $\boldsymbol{\xi}$ as the generalized coordinates. By substituting (4.14) into (4.24), $\boldsymbol{f_\xi}$ can be written as follows:

$$\boldsymbol{f_\xi} = \left(\boldsymbol{A}(\boldsymbol{\phi}) \cdot \boldsymbol{R_{\theta_2}}^{-1} \right)^T \begin{bmatrix} \boldsymbol{f} \\ \boldsymbol{f_\lambda} \end{bmatrix} \tag{4.25}$$

From the Euler–Lagrange equation, the following holds:

$$\frac{\mathrm{d}}{\mathrm{d}t} \left(\frac{\partial \mathcal{T}}{\partial \dot{\boldsymbol{\xi}}} \right) - \frac{\partial \mathcal{T}}{\partial \boldsymbol{\xi}} - \boldsymbol{f_\xi} = 0 \tag{4.26}$$

where $\mathcal{T}$ denotes the kinetic energy. We then obtain the equation of motion including the constraint forces as follows:

$$\boldsymbol{M}(\boldsymbol{\phi}) \boldsymbol{R_{\theta_2}}^{-1} \ddot{\boldsymbol{\xi}} + \boldsymbol{C}(\boldsymbol{\phi}, \dot{\boldsymbol{\xi}}) = \boldsymbol{A}^T(\boldsymbol{\phi}) \begin{bmatrix} \boldsymbol{f} \\ \boldsymbol{f_\lambda} \end{bmatrix} \tag{4.27}$$

where $\boldsymbol{M}(\boldsymbol{\phi})$ is an inertia matrix, and $\boldsymbol{C}(\boldsymbol{\phi}, \dot{\boldsymbol{\xi}})$ is a centrifugal matrix.

4.4.2 Procedure for planning dynamic skating motion

We do not plan the proposed system's motion by determining the state trajectory $\boldsymbol{\xi}(t) \in \mathbb{S}^1 \times \mathbb{S}^1 \times \mathbb{SE}(2)$, because the elements of $\boldsymbol{\xi}(t)$ cannot be determined independently; that is, $[\boldsymbol{A_{\lambda 1}} \ \boldsymbol{A_{\lambda 2}}] \cdot \boldsymbol{R_{\theta_2}}^{-1} \cdot \dot{\boldsymbol{\xi}} = \boldsymbol{0} \in \mathbb{R}^2$ must be satisfied for all t. Hence, we specify an initial state $\boldsymbol{\xi_0}$ and a trajectory of the generalized velocity $\boldsymbol{\gamma}(t) \in \mathbb{R}^3$; this allows the state trajectory $\boldsymbol{\xi}(t)$ to be determined as follows:

$$\boldsymbol{\xi}(t) = \boldsymbol{\xi_0} + \int_0^t \boldsymbol{F}(\boldsymbol{\xi}(\tau)) \cdot \boldsymbol{\gamma}(\tau) \mathrm{d}\tau \tag{4.28}$$

where $\boldsymbol{F}$ is a coordinate transformation matrix from $\boldsymbol{\gamma}$ to $\dot{\boldsymbol{\xi}}$, including the nonholonomic constraints; note that the existence of $\boldsymbol{F}$ is not guaranteed.

The selection of the coordinates of $\boldsymbol{\gamma}$ is arbitrary. With consideration of the symmetry of $\mathbb{SE}(2)$ and the existence of $\boldsymbol{F}$, we set the coordinates of $\boldsymbol{\gamma}$ as

$$\boldsymbol{\gamma} := \begin{bmatrix} \dot{\phi}_1 \\ \dot{\phi}_3 \\ \dot{x}_2 \cos(\theta_2) + \dot{y}_2 \sin(\theta_2) \end{bmatrix} \tag{4.29}$$

By defining $\boldsymbol{\gamma}$ as above, we ensure that $\boldsymbol{F}$ always exists. It is written as

$$\boldsymbol{F} = \boldsymbol{R_{\theta_2}} \begin{bmatrix} \boldsymbol{I_3} \\ -\boldsymbol{A_{\lambda 2}^{-1}} \boldsymbol{A_{\lambda 1}} \end{bmatrix} \tag{4.30}$$

Not all motions $\boldsymbol{\xi}(t)$ are mechanically admissible; the actuators' velocity and friction force must be finite. For example, it is expected that longitudinally accelerating motions in the singular posture would not be possible. Therefore, we derive sufficient conditions for a motion to be realized by a finite driving velocity $\boldsymbol{v}$ and finite friction forces $\boldsymbol{f}$ and $\boldsymbol{f_\lambda}$.

The driving velocity $\boldsymbol{v}$ is obtained in terms of $\boldsymbol{\gamma}$ as

$$\boldsymbol{v} = \begin{bmatrix} \boldsymbol{A_1} - \boldsymbol{A_2} \boldsymbol{A_{\lambda 2}^{-1}} \boldsymbol{A_{\lambda 1}} \end{bmatrix} \boldsymbol{\gamma} \tag{4.31}$$

Equation (4.31) holds for all time since $\boldsymbol{A_{\lambda 2}}$ is nonsingular by the assumption of the mechanical limit on joints. Therefore, if $\boldsymbol{\gamma}$ is sufficiently smooth against time, $\boldsymbol{v}$ is mechanically admissible.

The wheel forces $\boldsymbol{f}$ and $\boldsymbol{f_\lambda}$ are expressed by the dynamic equation (4.27):

$$\begin{bmatrix} \boldsymbol{f} \\ \boldsymbol{f_\lambda} \end{bmatrix} = \frac{\mathrm{adj}(\boldsymbol{A}^T) \left(\boldsymbol{M} \boldsymbol{R_{\theta_2}^{-1}} \ddot{\boldsymbol{\xi}} + \boldsymbol{C} \right)}{\det(\boldsymbol{A}^T)} \tag{4.32}$$

Since (4.32) holds only if $\det(\boldsymbol{A}^T) \neq 0$, careful handling with the singular posture is needed. We define $\boldsymbol{T_s}$ as the set of times at which the system is singular:

$$\boldsymbol{T_s} := \{ t > 0 \mid \det(\boldsymbol{A}(\boldsymbol{\xi}(t))) = 0 \} \tag{4.33}$$

Then for any time $t \notin \boldsymbol{T_s}$, the sufficient condition for $\boldsymbol{f}$ and $\boldsymbol{f_\lambda}$ to be mechanically admissible is clearly that $\boldsymbol{\gamma}$ be sufficiently smooth.

To achive admissible motion for the time $t \in \boldsymbol{T_s}$, we parameterize $\boldsymbol{\gamma}(t)$. We treat the dynamic skating motion as a motion in the longitudinal direction while the joint angle is being periodically changed. Thus, we parameterize the reference motion $\boldsymbol{\gamma}(t) = [\gamma_1(t) \ \gamma_2(t) \ \gamma_3(t)]^T$ by using a time-varying parameter $a(t)$ and constant parameters b and c as follows:

$$\phi_1(t) = \phi_1(0) + \int_0^t \gamma_1(\tau)\mathrm{d}\tau = a(t)\sin(bt + c)$$
$$\phi_3(t) = \phi_3(0) + \int_0^t \gamma_2(\tau)\mathrm{d}\tau = a(t)\sin(bt - c) \tag{4.34}$$

If we use the parameterizations (4.34), a sufficient condition for the wheel forces to be admissible is given by the following constraints:

$$a(t_s) \neq 0, \quad \left. \frac{\mathrm{d}\gamma_3(t)}{\mathrm{d}t} \right|_{t=t_s} = 0, \quad t_s \in \boldsymbol{T_s} \tag{4.35}$$

Substituting the reference motion into the numerator of (4.32) and the denominator of (4.32) leads the following equations:

$$\lim_{t \to t_s} \mathrm{adj}(\boldsymbol{A}^T)\left(\boldsymbol{M}\boldsymbol{R}_{\boldsymbol{\theta_2}}^{-1}\ddot{\boldsymbol{\xi}} + \boldsymbol{C}\right) = 0, \quad t_s \in \boldsymbol{T_s} \tag{4.36}$$

$$\lim_{t \to t_s} \det(\boldsymbol{A}^T) = 0, \quad t_s \in \boldsymbol{T_s} \tag{4.37}$$

Also the following equations hold:

$$\lim_{t \to t_s} \frac{\mathrm{d}\left(\mathrm{adj}(\boldsymbol{A}^T)\left(\boldsymbol{M}\boldsymbol{R}_{\boldsymbol{\theta_2}}^{-1}\ddot{\boldsymbol{\xi}} + \boldsymbol{C}\right)\right)}{\mathrm{d}t} \neq \pm\infty, \quad t_s \in \boldsymbol{T_s} \tag{4.38}$$

$$\lim_{t \to t_s} \frac{\mathrm{d}(\det(\boldsymbol{A}^T))}{\mathrm{d}t} \neq 0, \quad t_s \in \boldsymbol{T_s} \tag{4.39}$$

Thus, by the L'Hôpital's rule, the wheel forces $\boldsymbol{f}$ and $\boldsymbol{f_\lambda}$ are mechanically admissible if the generalized velocity $\boldsymbol{\gamma}$ satisfies (4.35).

4.4.3 Numerical verification of dynamic skating motion

The previous subsection described a design procedure for a motion in which the wheel velocity and the wheel friction force are finite even in the singular posture. We then verify it by a numerical simulation. We assume the moment of inertia of each link to be $J = 1/3$.

We describe a motion such that the two joint angles are opposite in phase, and the amplitude of undulation is constant. Note that the signs of ϕ_1 and ϕ_3 are reversed for the robot's posture because they are defined as $\phi_1 := -(\theta_2 - \theta_1)$ and $\phi_3 := \theta_3 - \theta_2$. The reference motion is established as shown in Fig. 4.10; it satisfies the admissibility conditions derived in the previous subsection. The simulation results for wheels' driving velocity and friction force are shown in Fig. 4.11, and top-view sequential depictions are shown in Fig. 4.12. From Fig. 4.11, it can be seen that the system moves with finite driving velocity and frictional force, including the singular posture.

4.5 Experiment

Finally, we demonstrate the kinematic-dual snake as an actual mechatronic system with the reference motion planned in Section 4.4.

4.5.1 Development

Fig. 4.13 shows the overview of the robot. The total length is 540 mm and the total mass is 1 kg. In order to ground all wheels in response to vehicle misalignment or ground unevenness of a few millimeters, we designed each link to be connected by a cylindrical pair. Each link is equipped with a microcontroller in order to follow the designed reference motion. Each microcontroller measures the joint angle and the motor velocity and communicates with other microcontrollers. The desired motor velocity is then determined from the reference motion and the present state so that the entire system follows the given reference motion. Each microcontroller also provides a current-velocity cascade feedback controller to ensure that each motor follows its desired velocity.
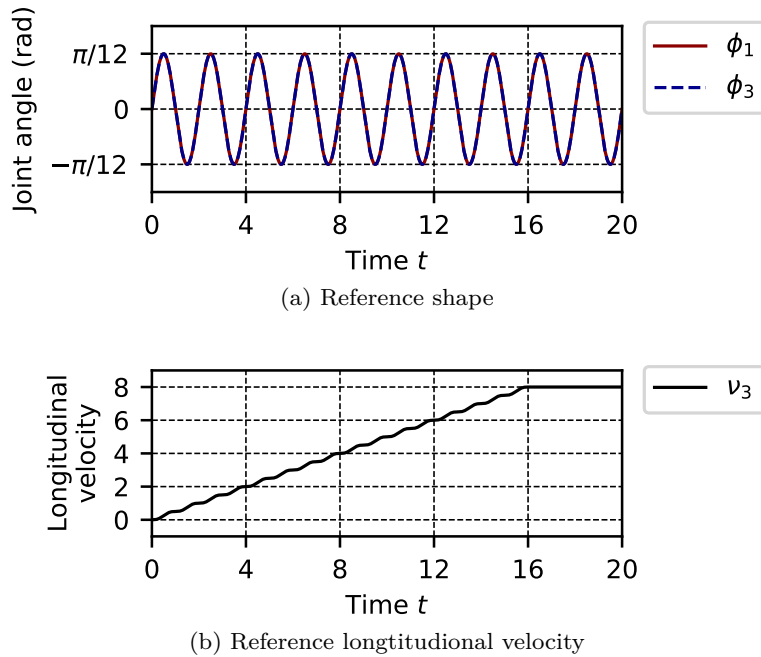
(a) Reference shape

(b) Reference longtitudional velocity

Fig. 4.10 Reference for the box-phase constant-amplitude undulation motion. Reference shapes ϕ_i are specified as in-phase sine waves.

(a) Driving velocities v_i

(b) Wheel forces $\boldsymbol{f}$ and $\boldsymbol{f}_{\boldsymbol{\lambda}}$
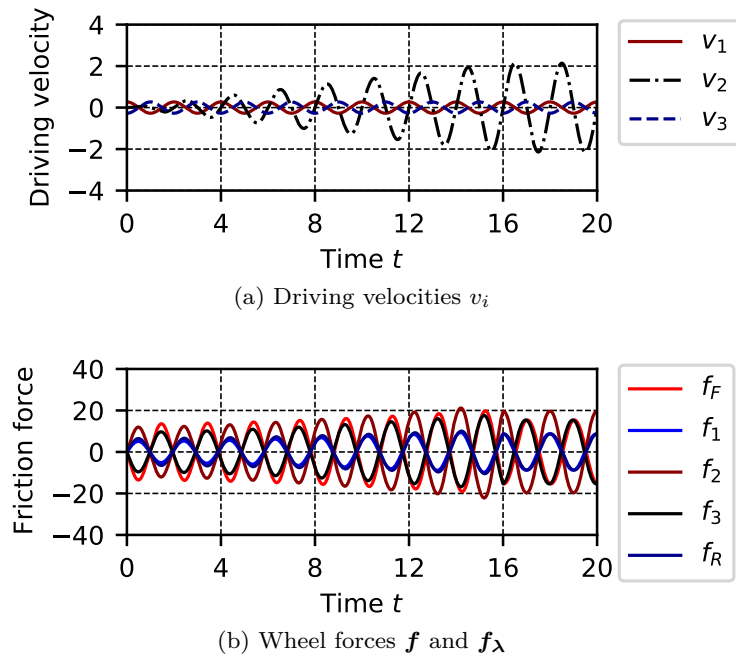
Fig. 4.11 Wheel velocities and forces are admissible throughout the box-phase constant-amplitude undulation motion.
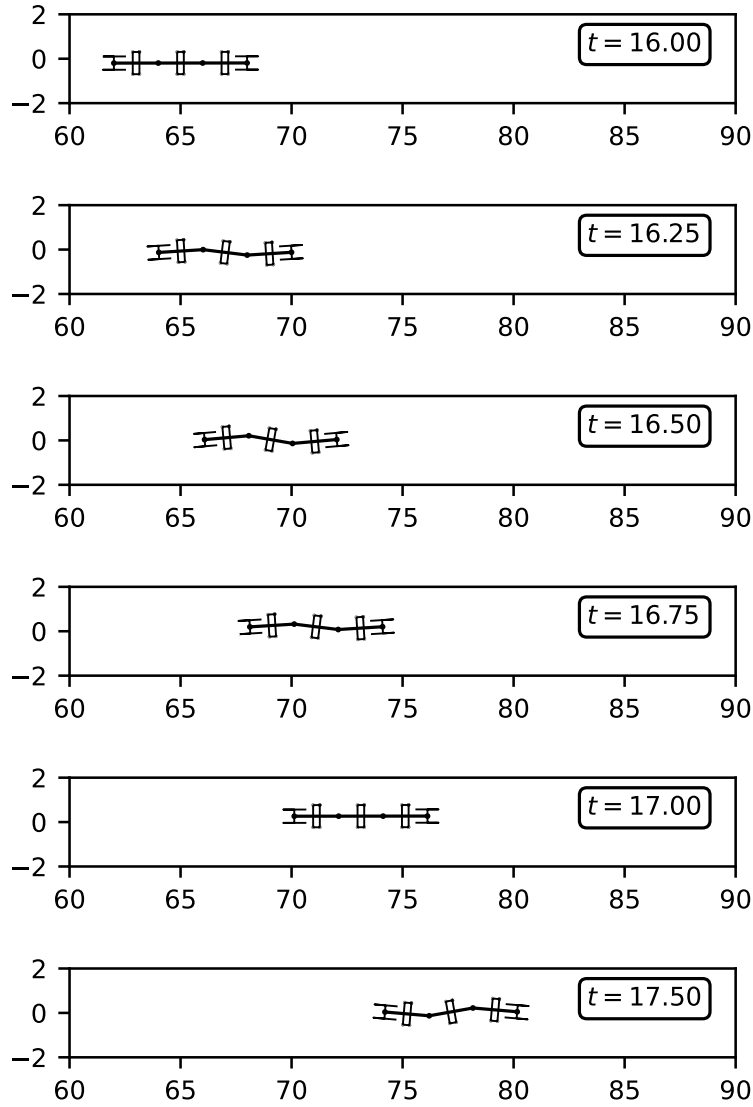
Fig. 4.12 Sequential depictions show the box-phase undulation motion.

4.5.2   Experiment setup and results

Then, we perform experiments. Based on the results of Section 4.4, we specify the reference motion by the joint angle and the longitudinal velocity, and the control was performed so that the actual joint angle and the actual longitudinal velocity follow the reference motion. The actual longitudinal velocity is estimated from the actual wheel velocities. A metal plate is used as the flooring material, and its flatness is within 1 mm approximately.

The first example is a box-phase undulation motion, where both joint reference angles are the same sinusoid, as shown in Fig. 4.15, and the longitudinal velocity is constant at 325 mm/s. Fig. 4.16 shows the snapshots of the box-phase motion. The time sequence of the joint angles is shown in Fig. 4.15. The actual motion does not fully follow the reference motion, but it can be seen that the robot indeed moves with undulation that includes the singular posture.
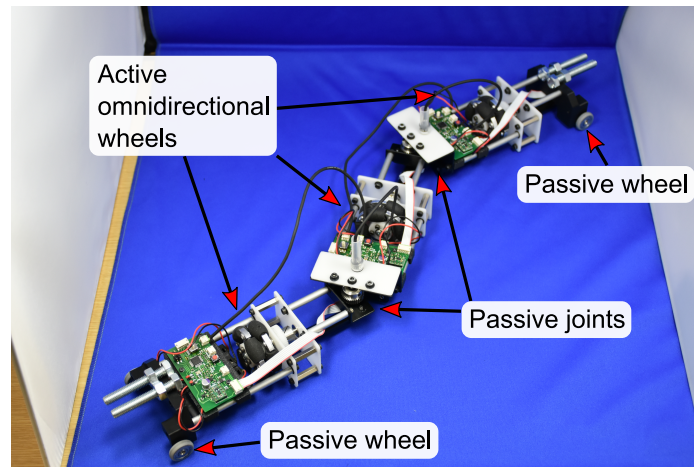
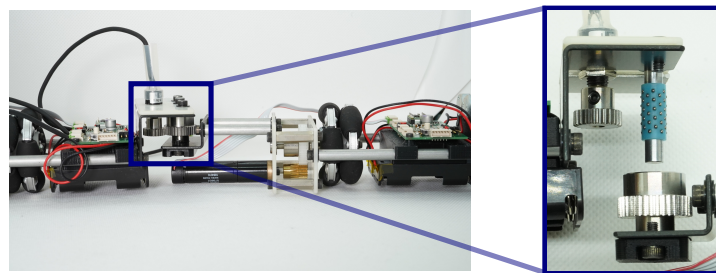Fig. 4.13   Mechatronic system of the kinematic-dual snake

Fig. 4.14   *Left:* A side view of the kinematic-dual snake is shown. DC geared motors rotate the omnidirectional wheels. *Right:* Exploded view of the joint is shown. Each passive joint is composed of cylindrical pair to make all wheels grounded. A potentiometer is attached to each joint to measure the joint angle via gears.
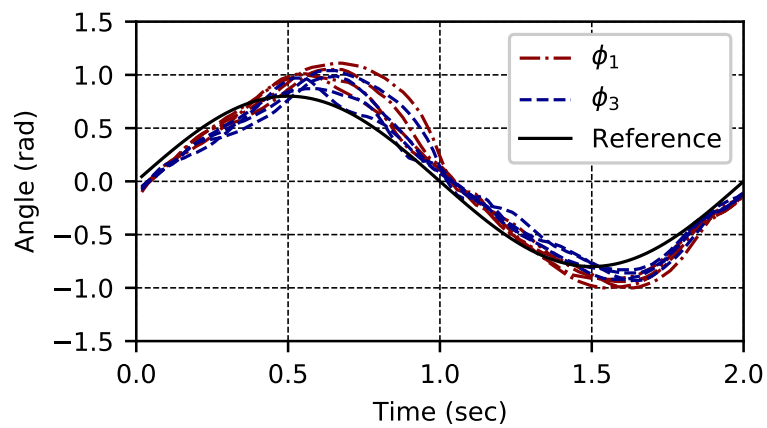

Fig. 4.15   The joint reference (desired) angle and the four cycles of actual angles in the box-phase motion are shown.
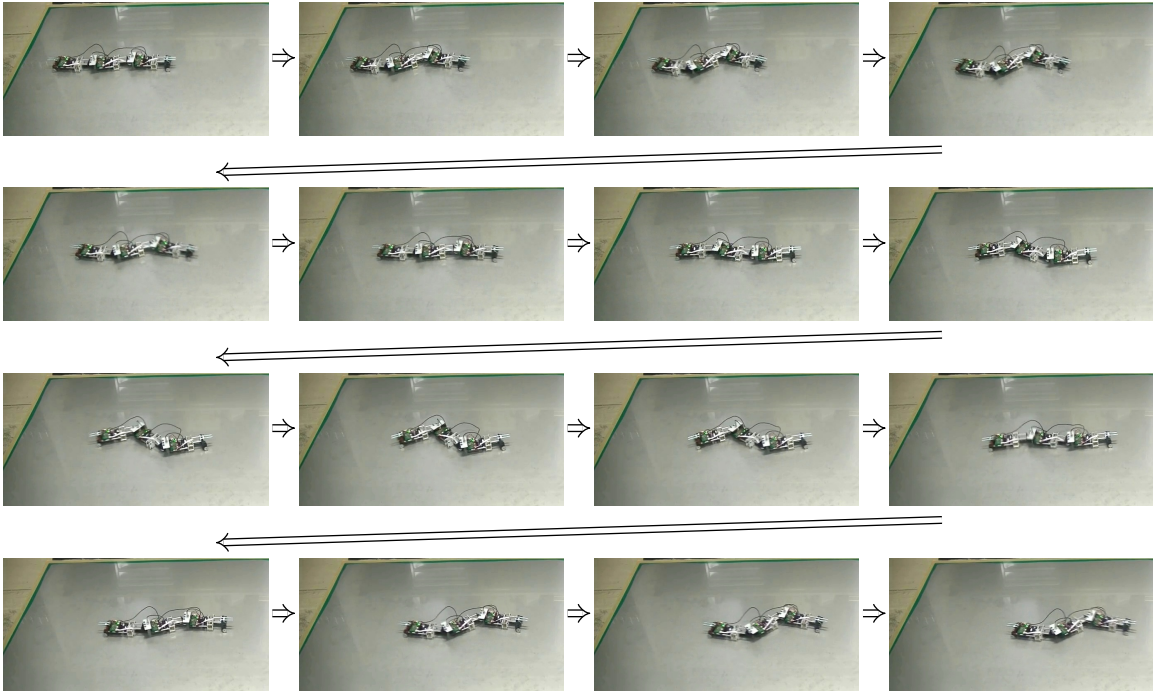
Fig. 4.16   Snapshots of a box-phase motion are shown. The time interval of the photos is 0.2 s; hence the total time is 3 s. The robot moves to the right with undulation, including the singular posture.

From this example, we can confirm that the kinematic-dual snake is not only a mathematical idea but also a realistic mechanical system.

Additional examples of motion are shown in Fig. 4.17 and Fig. 4.18, which are snapshots of a retrograde motion and a forward-wave motion, respectively. Each reference motion is a phase-only variation of the previous box-phase motion. Video clips of these experiments are provided in the electronic manuscript.

4.6   Conclusion and discussion

In this chapter, we have presented the notion of a kinematic-dual snake robot and shown its mechanical implementation. First, the kinematic-dual snake was introduced as a contrast to the original snake, especially for its mathematical relationship rather than mechanical relationship. Then, in Section 4.3 onward, we have shown that this kinematic-dual snake makes sense as a mechanical system through nonlinear controllability analysis, motion planning, development, and experiments.

The contrast between the original and the kinematic-dual snakes appears eminent when we increase the number of links. Table 4.1 shows the comparison of the DoFs of the both snakes. For the original snake with n links, (A) dimension of the total configuration space is $n + 2$ (corresponds to the position and orientation of the links). It has n passive wheels, which impose (B) n nonholonomic constraints. Thus the freedom of (C) instanteneous motion is $(n + 2) - (n) = 2$. Meanwhile, the robot has (D) $n - 1$ actuators at the joints. Thus there is a gap between (C) and (D). In the case of the kinematic-dual snake, (A) the configuration
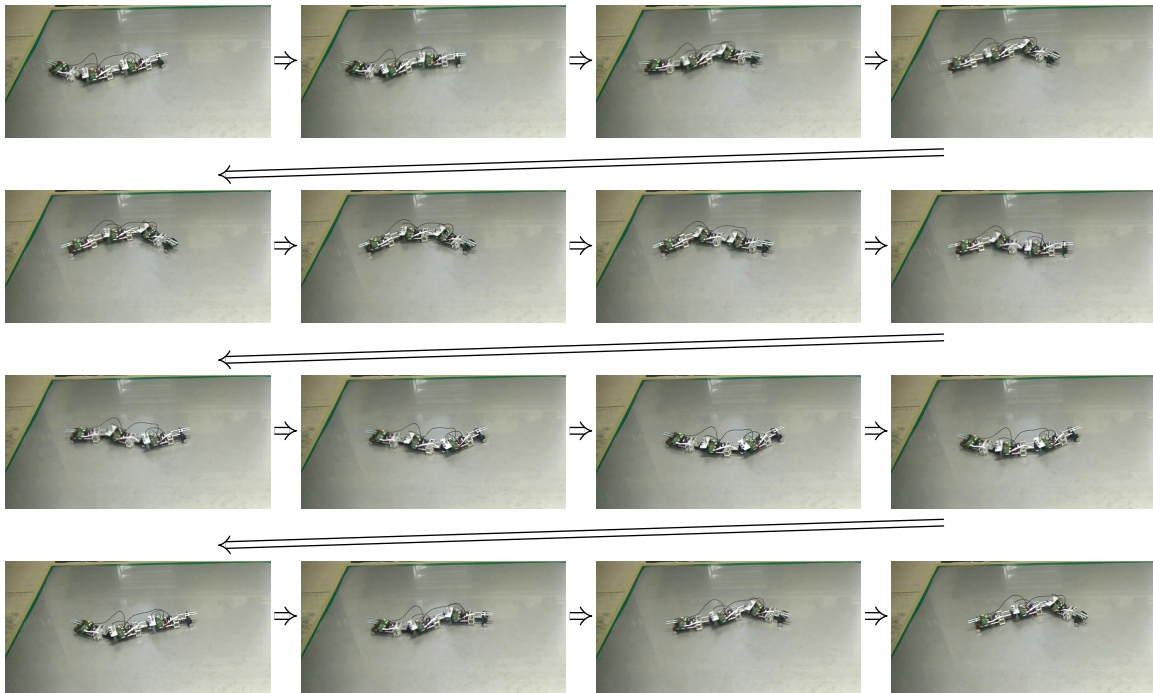
Fig. 4.17 Snapshots of a retrograde motion are shown. The time interval of the photos is 0.2 s; hence the total time is 3 s. The robot moves to the right with retrograde undulation.
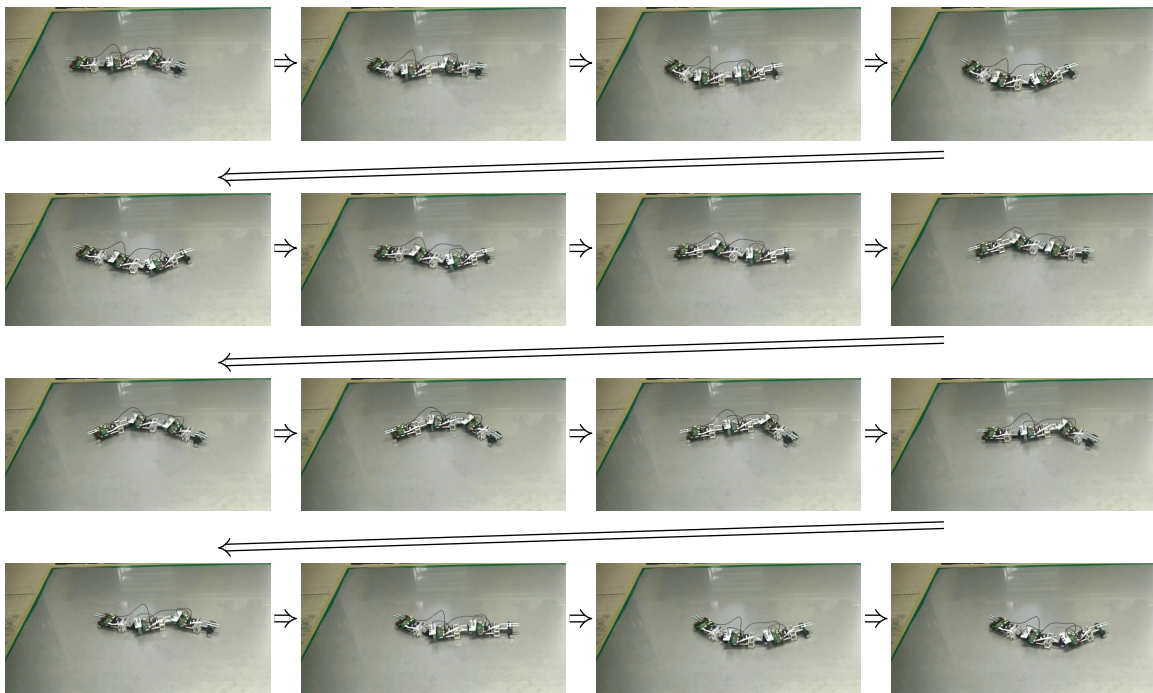

Fig. 4.18 Snapshots of a forward-wave motion are shown. The time interval of the photos is 0.2 s; hence the total time is 3 s. The robot moves to the right with forward-wave undulation.

Table 4.1   The table shows a comparison of DoFs and the number of active actuators with n links. For the kinematic-dual snake, the dimension of instantaneous motion is n, and the same number of actuators are equipped.

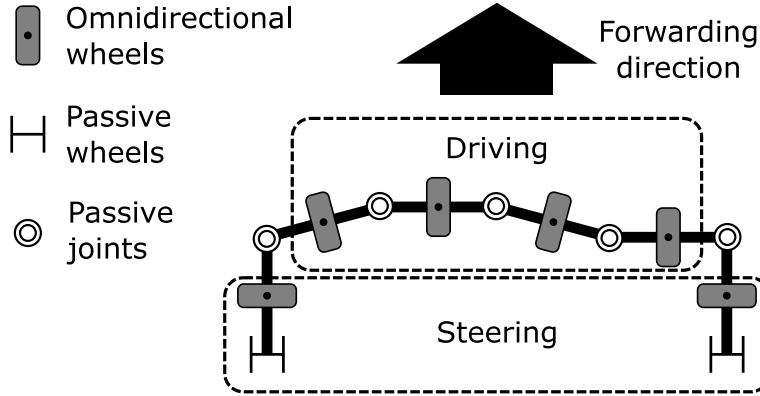| Type of robot	(A) Configuration space	(B) Nonholonomic constraints	(C) Instantaneous motion	(D) actuators
Original snake	$n + 2$	n	2	$n - 1$
Kinematic-dual snake	$n + 2$	2	n	n

Fig. 4.19   One example of locomotion shape by the kinematic-dual snake is a U shape. The omnidirectional wheels at both ends perform steering, and the wheels in the center perform driving. Of course, the snake can be transformed as desired in this posture.

space is $n + 2$ as the same as the original one. It has only 2 passive wheels at the ends, imposing (B) 2 nonholonomic constraints. Thus the freedom of (C) instanteneous motion is $(n + 2) - (2) = n$. Meanwhile, the robot has (D) n omnidirectional wheels at the links, which is equal to (C).

This difference allows the kinematic-dual snake to travel and transform independently by n actuators. This is expressed in equations (32)-(34) for the 3-link case. In the n-link case, for arbitrary desired $n - 1$ joint angular velocities and longitudinal velocities, there exist the actuator inputs that achieve such motions. In the skating motion discussed in Section 5, undulation by sinusoid is assigned, but this is just for simplicity, and any joint angular velocity and longitudinal velocity, including those other than sinusoidal, can be realized. As an example of locomotion without undulation, we can conceive a U shape locomotion, as shown in Figure 4.19.

The idea of the kinematic-dual snake originates from the control-theoretical point of view to solve the disadvantages of the original snake robot. The main feature of the kinematic-dual snake in terms of the mechanical design is that the axial drive and joints are passive, and only the lateral drive of each link is manipulated. This feature provides the following advantages.

1. More manipulability: there are only two nonholonomic constraints, and the actuators are mounted so that the driving force acts laterally to the links, enabling both joint angle manipulation and traveling.

2. Just-enough actuators: The number of actuators, n, corresponds to the instantaneous

    degrees of motion with no excess nor deficiency. All the actuators will contribute to the driving force with less conflict among them.

3. Distributed traction: it can maintain the traction (contact force with the ground) across the whole body.

Overall, the proposed robot can improve its manipulability while maintaining the advantages of the string-like body. The concept of the kinematic-dual snake was proven in Section 3 and onward. Practical robots utilizing this concept should be developed for the next step. The authors expect this idea would contribute to tasks that require both joint angle manipulation and traveling, such as transportation with wrapping around an object.

As a future work, it is worth pursuing a potential advantage of the proposed robot in coping with uncontrolled environments. It is a hypothesis for the time being though, the proposed robot would be suitable uneven terrain than the original snake robots, thanks to the number of "active" wheels along the body. In order to verify this issue, we should carefully re-design the joint mechanism and motion algorithms so that it can contact with non-flat surface.

Chapter 5

Conclusion

In the works of this thesis, I mainly dealt with two issues concerned with the "first-order systems," one of which contributes to control theory, while the other contributes to the mechanism design. As a contribution to control theory, this thesis focused on the three-input Brockett's canonical system and described that the helix paths satisfy a specific shortest condition. To contribute to mechanism design, I focused on the degrees of freedom in kinematics and proposed a dual snake robot as a counterpart to the original snake robot. I confirmed that the proposed snake robot could move and transform its posture independently, theoretically, and experimentally.

I tackled these two different issues based on my perspective that advancing both control and mechanism is necessary for the social implementation of nonholonomic systems. This is because the studies of the control and mechanism of nonholonomic systems are essential to motivate each other. This is just like "chicken first or egg first." One solution to advance the research under this structure is to advance both simultaneously.

Although each topic of this study is still a ways off, its ideas and directions are essential for advancing nonholonomic systems. I hope this work will be help in future research and development.

Bibliography

[1] R. M. Murray and S. S. Sastry, "Nonholonomic motion planning: steering using sinusoids," *IEEE Transactions on Automatic Control*, vol. 38, no. 5, pp. 700–716, 1993.

[2] B. He, S. Wang, and Y. Liu, "Underactuated robotics: a review," *International Journal of Advanced Robotic Systems*, vol. 16, no. 4, pp. 1–29, 2019.

[3] H. Nijmeijer and A. J. V. der Schaft, *Nonlinear Dynamical Control Systems*. Springer, 1990.

[4] A. Isidori, *Nonlinear Control Systems*. Springer, 1995.

[5] A. M. Bloch, J. Baillieul, P. Crouch, and J. Marsden, *Nonholonomic Mechanics and Control*. Springer, 2003.

[6] S. Sastry, *Nonlinear Systems: Analysis, Stability, and Control*. Springer, 1999.

[7] R. Hermann and A. Krener, "Nonlinear controllability and observability," *IEEE Transactions on Automatic Control*, vol. 22, no. 5, pp. 728–740, 1977.

[8] G. Walsh, D. Tilbury, S. Sastry, R. Murray, and J.-P. Laumond, "Stabilization of trajectories for systems with nonholonomic constraints," *IEEE Transactions on Automatic Control*, vol. 39, no. 1, pp. 216–222, 1994.

[9] A. Astolfi, "Discontinuous control of nonholonomic systems," *Systems & Control Letters*, vol. 27, no. 1, pp. 37–45, 1996.

[10] P. Morin and C. Samson, "Time-varying exponential stabilization of a rigid spacecraft with two control torques," *IEEE Transactions on Automatic Control*, vol. 42, no. 4, pp. 528–534, 1997.

[11] K. Y. Pettersen and O. Egeland, "Time-varying exponential stabilization of the position and attitude of an underactuated autonomous underwater vehicle," *IEEE Transactions on Automatic Control*, vol. 44, no. 1, pp. 112–115, 1999.

[12] P. Morin and C. Samson, "Practical stabilization of driftless systems on Lie groups: the transverse function approach," *IEEE Transactions on Automatic Control*, vol. 48, no. 9, pp. 1496–1508, 2003.

[13] K. Fujimoto, S. Sakai, and T. Sugie, "Passivity based control of a class of Hamiltonian systems with nonholonomic constraints," *Automatica*, vol. 48, no. 12, pp. 3054–3063, 2012.

[14] N. E. Leonard and P. S. Krishnaprasad, "Motion control of drift-free, left-invariant systems on Lie groups," *IEEE Transactions on Automatic Control*, vol. 40, no. 9, pp. 1539–1554, 1995.

[15] H. Khennouf and C. C. De Wit, "On the construction of stabilizing discontinuous controllers for nonholonomic systems," *IFAC Proceedings Volumes*, vol. 28, no. 14, pp. 667–672, 1995.

[16] R. W. Brockett, "Control theory and singular riemannian geometry," in *New Directions in Applied Mathematics*. Springer, 1982, pp. 11–27.

[17] R. Brockett, "Lie theory and control systems defined on spheres," *SIAM Journal on Applied Mathematics*, vol. 25, no. 2, pp. 213–225, 1973.

[18] J. Baillieul, "Geometric methods for nonlinear optimal control problems," *Journal of*

Optimization Theory and Applications, vol. 25, no. 4, pp. 519–548, 1978.

[19] S. S. Sastry and R. Montgomery, "The structure of optimal controls for a steering problem," in *Nonlinear Control Systems Design 1992*. Elsevier, 1993, pp. 135–140.

[20] V. Jurdjevic, *Geometric Control Theory*. Cambridge university press, 1997.

[21] ——, *Optimal Control and Geometry: Integrable Systems*. Cambridge University Press, 2016.

[22] J. P. Ostrowski, J. P. Desai, and V. Kumar, "Optimal gait selection for nonholonomic locomotion systems," *The International Journal of Robotics Research*, vol. 19, no. 3, pp. 225–237, 2000.

[23] K. Spindler, "Optimal attitude control of a rigid body," *Applied Mathematics and Optimization*, vol. 34, no. 1, pp. 79–90, 1996.

[24] H. C. Henninger and J. D. Biggs, "Optimal under-actuated kinematic motion planning on the ϵ-group," *Automatica*, vol. 90, pp. 185–195, 2018.

[25] G. C. Walsh, R. Montgomery, and S. S. Sastry, "Optimal path planning on matrix Lie groups," in *Proceedings of 1994 33rd IEEE Conference on Decision and Control*, vol. 2. IEEE, 1994, pp. 1258–1263.

[26] J. Biggs, W. Holderbaum, and V. Jurdjevic, "Singularities of optimal control problems on some 6-D Lie groups," *IEEE Transactions on Automatic Control*, vol. 52, no. 6, pp. 1027–1038, 2007.

[27] R. M. Murray, Z. Li, and S. S. Sastry, *A Mathematical Introduction to Robotic Manipulation*. CRC press, 1994.

[28] R. W. Brockett, "Asymptotic stability and feedback stabilization," in *Differential Geometric Control Theory: Proceedings of the conference held at Michigan Technological University, June 28-July 2, 1982*. Birkhauser, 1983, pp. 181–191.

[29] J. Gray, "The mechanism of locomotion in snakes," *Journal of experimental biology*, vol. 23, no. 2, pp. 101–120, 1946.

[30] S. Hirose, *Biologically Inspired Robots: Snake-like Locomotors and Manipulators*. Oxford University Press, 1993.

[31] S. Hirose and H. Yamada, "Snake-like robots [tutorial]," *IEEE Robotics & Automation Magazine*, vol. 16, no. 1, pp. 88–98, 2009.

[32] P. Prautsch and T. Mita, "Control and analysis of the gait of snake robots," in *Proceedings of the 1999 IEEE International Conference on Control Applications*, vol. 1. IEEE, 1999, pp. 502–507.

[33] P. Prautsch, T. Mita, and T. Iwasaki, "Analysis and control of a gait of snake robot," *IEEJ Transactions on Industry Applications*, vol. 120, no. 3, pp. 372–381, 2000.

[34] H. Date, Y. Hoshi, and M. Sampei, "Locomotion control of a snake-like robot based on dynamic manipulability," in *Proceedings of IEEE/RSJ International Conference on Intelligent Robots and Systems*, vol. 3, 2000, pp. 2236–2241.

[35] P. Liljeback, I. U. Haugstuen, and K. Y. Pettersen, "Path following control of planar snake robots using a cascaded approach," *IEEE Transactions on Control Systems Technology*, vol. 20, no. 1, pp. 111–126, 2012.

[36] S. D. Kelly and R. M. Murray, "Geometric phases and robotic locomotion," *Journal of Robotic Systems*, vol. 12, no. 6, pp. 417–431, 1995.

[37] J. Ostrowski and J. Burdick, "The geometric mechanics of undulatory robotic locomotion," *The international journal of robotics research*, vol. 17, no. 7, pp. 683–701, 1998.

[38] M. Ishikawa, "Iterative feedback control of snake-like robot based on principal fibre bundle modelling," *International Journal of Advanced Mechatronic Systems*, vol. 1, no. 3, pp. 175–182, 2009.

[39] M. Ishikawa, K. Owaki, M. Shinagawa, and T. Sugie, "Control of snake-like robot based

on nonlinear controllability analysis," in *Proceedings of IEEE International Conference on Control Applications*, 2010, pp. 1134–1139.

[40] M. Saito, M. Fukaya, T. Iwasaki *et al.*, "Modeling, analysis, and synthesis of serpentine locomotion with a multilink robotic snake," *IEEE control systems magazine*, vol. 22, no. 1, pp. 64–81, 2002.

[41] F. Matsuno and K. Mogi, "Redundancy controllable system and control of snake robots based on kinematic model," in *Proceedings of the 39th IEEE Conference on Decision and Control*, vol. 5. IEEE, 2000, pp. 4791–4796.

[42] S. Ma, Y. Ohmameuda, K. Inoue, and B. Li, "Control of a 3-dimensional snake-like robot," in *2003 IEEE International Conference on Robotics and Automation*, vol. 2. IEEE, 2003, pp. 2067–2072.

[43] A. A. Transeth, R. I. Leine, C. Glocker, and K. Y. Pettersen, "3-d snake robot motion: nonsmooth modeling, simulations, and experiments," *IEEE transactions on robotics*, vol. 24, no. 2, pp. 361–376, 2008.

[44] M. Tanaka and K. Tanaka, "Singularity analysis of a snake robot and an articulated mobile robot with unconstrained links," *IEEE Transactions on Control Systems Technology*, vol. 24, no. 6, pp. 2070–2081, 2016.

[45] H. Ohno and S. Hirose, "Design of slim slime robot and its gait of locomotion," in *Proceedings 2001 IEEE/RSJ International Conference on Intelligent Robots and Systems*, vol. 2. IEEE, 2001, pp. 707–715.

[46] C. Behn, L. Heinz, and M. Krüger, "Kinematic and dynamic description of non-standard snake-like locomotion systems," *Mechatronics*, vol. 37, pp. 1–11, 2016.

[47] H. Kimura and S. Hirose, "Development of genbu: Active wheel passive joint articulated mobile robot," in *IEEE/RSJ International Conference on Intelligent Robots and Systems*, vol. 1. IEEE, 2002, pp. 823–828.

[48] T. Kamegawa, T. Yarnasaki, H. Igarashi, and F. Matsuno, "Development of the snake-like rescue robot" kohga"," in *IEEE International Conference on Robotics and Automation, 2004. Proceedings. ICRA'04. 2004*, vol. 5. IEEE, 2004, pp. 5081–5086.

[49] M. Arai, T. Takayama, and S. Hirose, "Development of" souryu-iii": connected crawler vehicle for inspection inside narrow and winding spaces," in *2004 IEEE/RSJ International Conference on Intelligent Robots and Systems*, vol. 1. IEEE, 2004, pp. 52–57.

[50] J. Borenstein, G. Granosik, and M. Hansen, "The omnitread serpentine robot: design and field performance," in *Unmanned Ground Vehicle Technology VII*, vol. 5804. SPIE, 2005, pp. 324–332.

[51] M. Hara, S. Satomura, H. Fukushima, T. Kamegawa, H. Igarashi, and F. Matsuno, "Control of a snake-like robot using the screw drive mechanism," in *Proceedings 2007 IEEE International Conference on Robotics and Automation.* IEEE, 2007, pp. 3883–3888.

[52] H. Fukushima, S. Satomura, T. Kawai, M. Tanaka, T. Kamegawa, and F. Matsuno, "Modeling and control of a snake-like robot using the screw-drive mechanism," *IEEE Transactions on Robotics*, vol. 28, no. 3, pp. 541–554, 2012.

[53] Y. Takagi, Y. Sueoka, M. Ishikawa, and K. Osuka, "Analysis and control of a snake-like robot with controllable side-thrust links," in *Proceedings of Asian Control Conference*, 2017, pp. 754–759.

[54] ——, "Snake-like robot with controllable side-thrust links: Dynamical modeling and a variable undulation motion," in *Proceedings of IEEE/ASME International Conference on Advanced Intelligent Mechatronics*, 2018, pp. 63–68.

[55] Y. Takagi, M. Ishikawa, and K. Osuka, "Development and control experiment of a snake-like robot with controllable side-thrust links," *IFAC-PapersOnLine*, vol. 52, no. 15, pp. 229–234, 2019.

Pulication list

Journal papers

[1] Y. Takagi, M. Ishikawa, and K. Osuka, "A kinematic-dual snake robot: Undulatory mobile robot driven by controllable side-thrust links," *Mechatronics*, vol. 90, p. 102944, 2023.

[2] Y. Takagi and M. Ishikawa, "Optimal Path Planning on the Three-input Six-dimensional Brockett's Canonical System," *IEEE Access*, vol. 11, pp. 88618–88626, 2023.

Refereed international conference papers

[1] Y. Takagi, Y. Sueoka, M. Ishikawa, and K. Osuka, "Analysis and control of a snake-like robot with controllable side-thrust links," in *Proceedings of Asian Control Conference*, 2017, pp. 754–759.

[2] Y. Takagi, Y. Sueoka, M. Ishikawa, and K. Osuka, "Snake-like robot with controllable side-thrust links: Dynamical modeling and a variable undulation motion," in *Proceedings of IEEE/ASME International Conference on Advanced Intelligent Mechatronics*, 2018, pp. 63–68.

[3] Y. Takagi, M. Ishikawa, and K. Osuka, "Development and control experiment of a snake-like robot with controllable side-thrust links," in *Proceedings of 8th IFAC Symposium on Mechatronic Systems MECHATRONICS 2019*, vol. 52, no. 15, pp. 229–234, 2019.

Domestic conference papers

[1] 高木勇樹，末岡裕一郎，大須賀公一，"複数の法線方向駆動機構による蛇行ロコモーションの実現に向けて"，日本機械学会ロボティクス・メカトロニクス講演会（ROBOMECH2017），2017.

[2] 高木勇樹，石川将人，"劣駆動キネマティックシステムにおける拘束と入力の役割-双対なヘビロボットの事例研究"，第 9 回 制御部門マルチシンポジウム（MSCS2022），2022.